Visualising the cytoskeletal machinery in neuronal growth cones using cryo-electron tomography

Running Title: Cryo-ET of neuronal growth cones

Joseph Atherton[1, 2*], Melissa Stouffer[3,4,5,6], Fiona Francis[3,4,5] and Carolyn A. Moores[2*]

[1] Randall Centre for Cell and Molecular Biophysics, King's College, London, United Kingdom.
[2] Institute of Structural and Molecular Biology, Birkbeck, University of London, London, United Kingdom.
[3] INSERM UMR-S 1270, 17 Rue du Fer a` Moulin, 75005 Paris, France,
[4]Sorbonne University, 4 Place Jussieu, 75005 Paris, France.
[5] Institut du Fer a` Moulin, 17 Rue du Fer a` Moulin, 75005 Paris, France.
[6] Institute of Science and Technology Austria, Am campus 1, 3400 Klosterneuberg, Austria.

* corresponding authors: joseph.atherton@kcl.ac.uk; c.moores@mail.cryst.bbk.ac.uk

Key words: neuron, growth cone, cytoskeleton, actin, microtubule, doublecortin

Summary statement

Cryo-electron tomographic reconstruction of neuronal growth cone subdomains reveals distinctive F-actin and microtubule cytoskeleton architectures and modulation at molecular detail.

ABSTRACT

Neurons navigate long distances and extend axons to form the complex circuitry of the mature brain. This depends on the coordinated response and continuous remodelling of the microtubule and F-actin networks in the axonal growth cone. Growth cone architecture remains poorly understood at nanoscales. We therefore investigated mouse hippocampal neuron growth cones using cryo-electron tomography to directly visualise their three-dimensional subcellular architecture with molecular detail. Our data show the hexagonal arrays of actin bundles that form filopodia penetrate the growth cone interior and terminate in the transition zone. We directly observe the modulation of these and other growth cone actin bundles by alteration of individual F-actin helical structures. Blunt-ended microtubules predominate in the growth cone, frequently contain lumenal particles and carry lattice defects. Investigation of the effect of absence of doublecortin, a neurodevelopmental cytoskeleton regulator, on growth cone cytoskeleton shows no major anomalies in overall growth cone organisation or in F-actin subpopulations. However, our data suggest that microtubules sustain more structural defects, highlighting the importance of microtubule integrity during growth cone migration.

INTRODUCTION

During development of the nervous system, neurons first form primary extensions that direct cell migration, and then extend axons to form synapses. These pathfinding processes are directed by the axonal growth cone, a dynamic and responsive structure at the end of the axon (Fig. 1A). Growth cone movement in response to guidance cues is driven by an integrated network of microtubule (MT) and actin filaments (F-actin), and regulated by a large array of cytoskeleton binding proteins. Molecular malfunction in the growth cone causes aberrant axonal pathfinding and – ultimately - incorrect wiring of the nervous system, and is the basis of a number of neurodevelopmental disorders including a range of intellectual disability conditions, autism and schizophrenia (Bakos et al., 2015; Kim and Kim, 2020; Stoeckli, 2018). For example, mutations in the protein doublecortin (DCX in humans, Dcx in mouse), which is a regulator of both growth cone F-actin and MT organisation (Deuel et al., 2006; Friocourt et al., 2003; Fu et al., 2013; Jean et al., 2012; Tint et al., 2009), cause a neurodevelopmental lissencephaly associated with cortical disorganisation and abnormal neuronal circuit formation (reviewed in (Wynshaw-Boris et al., 2010)). Understanding the organisation and regulation of the neuronal growth cone cytoskeleton can thus shed light both on the molecular basis of numerous diseases and potential therapeutic strategies for axonal regeneration after nervous system injury or disease (Blanquie and Bradke, 2018; Roig-Puiggros et al., 2020).

Distinct growth cone regions have been characterised based on their appearance, organelle distribution and cytoskeletal composition (Fig. 1B). The axon shaft that precedes the growth cone is filled with parallel, tightly bundled MTs - large organelles such as mitochondria are common and F-actin is relatively sparse (Dent et al., 2011). The axon connects with the central domain (C-domain) of the growth cone, which includes the so-called axon wrist, and, while also containing large organelles and MTs, C-domain MTs are more dispersed and dynamic (Blanquie and Bradke, 2018). The front region of the growth cone - the peripheral domain (P-domain) - is flat and organelle-free. It is constituted of F-actin bundle-containing protrusions called filopodia at its very edge, together with the branched F-actin network containing lamellipodium from which the filopodia protrude. The P-domain is

separated from the C-domain by the transition zone (T-zone) which, as its name suggests, is a region of transition between the F-actin dominated outer regions of the growth cone and the MT-rich axon-proximal regions. Contractile F-actin arcs formed by non-muscle myosin II run parallel to the front of the growth cone in the T-zone and help drive cellular motility (Burnette et al., 2008; Burnette et al., 2007; Schaefer et al., 2002; Zhang et al., 2003). MTs are only rarely observed growing from the T-zone into the P-domain, and they are often guided by interactions with F-actin bundles (Gordon-Weeks, 1991; Sabry et al., 1991; Schaefer et al., 2002; Schaefer et al., 2008). Furthermore, MTs that are found in the periphery of the growth cone are dynamic and unstable - exploratory MTs that are linked to F-actin retrograde flow are often induced to buckle and break in the T-zone (Schaefer et al., 2002; Schaefer et al., 2008; Waterman-Storer and Salmon, 1997).

Directional growth cone extension is driven by guidance cues that act at focal adhesions to restrict F-actin bundle retrograde flow (Bard et al., 2008; Chan and Odde, 2008; Suter and Forscher, 1998), allowing actin-associated MT retention and subsequent delivery of components and organelles required for axonal extension (Brown and Bridgman, 2003; Burnette et al., 2007; Forscher and Smith, 1988; Medeiros et al., 2006; Schaefer et al., 2002; Schaefer et al., 2008; Williamson et al., 1996; Zhou et al., 2002). Coordination between the MT and F-actin networks are thus critical for growth cone extension, but a number of open questions remain concerning the molecular basis for their individual regulation and their coordination. The precise organisation of non-filopodia P-domain F-actin and its connectivity and communication with the T-zone is not well understood. In particular, the mechanism by which filopodial F-actin bundles are disassembled, and how actin arcs are generated in the T-zone is not clear. In addition, it is not known whether different growth cone MT populations have distinct structural signatures, and, although the involvement of a number of MT-actin crosslinkers have been proposed (Geraldo and Gordon-Weeks, 2009; Lowery and Van Vactor, 2009), how peripheral MTs in growth cones associate with or are influenced by different arrays of F-actin is currently unclear at the molecular level. Nanoscale insights into neuronal growth cone organisation can provide key insights to address some of these outstanding questions.

Cryo-electron tomography (cryo-ET) provides a window into the growth cone interior by enabling visualisation of intact frozen-hydrated cellular samples; three-dimensional (3D) reconstruction enables ultrastructural characterisation of molecular components *in situ* (Turk and Baumeister, 2020). While growth cone ultrastructure has been extensively studied using fixed and heavy metal stained samples (e.g. (Bridgman and Dailey, 1989; Brown and Bridgman, 2009; Efimova et al., 2020; Yamada et al., 2013), these methods can introduce artefacts and impose limits on resolution. We therefore used cryo-ET and machine learning-based segmentation and visualisation to investigate the complex molecular organisation of sub-compartments within mouse hippocampal neuron growth cones and the part of the axon that leads in to them. We focused particularly on their underlying cytoskeletal architectures vital to axon pathfinding. We also compared the growth cone ultrastructure in mouse wild-type neurons with those of Dcx knockout neurons, to evaluate the effect of Dcx loss on the cytoskeleton, and thereby provide new insights into cytoskeleton defects that potentially contribute to neurodevelopmental disorders.

RESULTS

Cryo-electron tomography of primary hippocampal neuron growth cones

We chose mouse primary hippocampal neurons as a model system to study growth cone architecture because the biology of their growth cone formation and function is well studied, and because the Dcx knockout phenotype in mice manifests itself most prominently in a hippocampal malformation (Corbo et al., 2002; Kappeler et al., 2007). After 2-3 days of *in vitro* culture on laminin/poly-D-lysine, these cells exhibit several short minor dendritic processes, together with an extended axon, tipped by a growth cone, the so-called stage 3 morphology (Fig. 1A; reviewed in (Banker, 2018). The distinct intracellular organisation of these growth cones, in which the axon shaft and C-domain are packed with MTs, while the P-domain is dominated by F-actin (Fig. 1B), is very clear. Dcx mostly colocalises with MTs towards the outer ends of processes and in the growth cone C-domain (Bielas et al., 2007), but less intense Dcx staining is also seen in the P-domain colocalised with actin (Fig. 1A, B), consistent with previous reports (Fu et al., 2013; Tint et al., 2009).

We used cryo-ET to examine the interplay between neuronal cytoskeleton components at the molecular level. Mouse primary hippocampal neurons were grown on laminin/poly-D-lysine-treated holey carbon electron microscopy (EM) grids for 2-3 days until the characteristic stage 3 morphology was observed using phase contrast light microscopy. Grids were vitrified, imaged using cryo-ET, and growth cones were readily identified at low magnification EM by their characteristic appearance (Fig. 1C; Sup. Fig. 1A, B). Because these neuronal regions are typically no thicker (in z) than 500 nm, consistent and uniform vitrification was observed, and electron transmission was sufficient to allow tilt series collection. 30 tilt series of a ~2.15 by 2.15 µm field of view were collected from different growth cones regions (derived from 12 neurons, 7 different mice and 10 different grids) that lay over 2 µm diameter holes in the carbon substrate of the EM grid (Fig. 1C, D). 3D tomographic volumes were calculated from these tilt series, allowing clear visualisation of the interior of the neuron, including MTs, F-actin and membrane-bound organelles (Fig. 1D & Sup. Video 1).

Visualisation of the axonal growth cone molecular landscape

We used neural network-based approaches to perform semi-automated segmentation of the growth cone tomograms (see Methods), enabling 3D visualisation of their molecular organisation (Fig. 2). This provided us, first, with an overview of the distribution of neuronal components in different regions of the growth cones. While the pre-cone axon is densely packed with MT bundles (Sup. Fig. 1C), MTs also dominate the growth cone C-domain but are more loosely packed - as a consequence, they exhibit more variable orientations with respect to the membrane and a greater range of curvatures (Fig. 2A). Mitochondria and vesicles of different size are prevalent in the C-domain, while endoplasmic reticulum (ER) networks are less frequent compared to the axon (Fig. 2A). Individual ribosomes and clustered polysomes are common in the C-domain although their distribution is not obviously correlated with cytoskeletal components (Fig. 2A, middle, right, red features). Actin filaments are relatively sparse and predominantly observed at the cortex (Fig. 2A, right).

In contrast to the C-domain, the T-zone is dominated by F-actin; MTs are only occasionally observed and they are neither bundled nor uniformly oriented (Fig. 2B). This region of the growth cone is full of numerous, tight F-actin bundles, together with a looser network of other actin filaments, described in more detail below. Large organelles are infrequent in the T-zone but vesicular organelles, membranous reticulum and small vesicles are present (Fig. 2B). Ribosomes are distributed throughout the T-zone but, in contrast to the C-domain, polysome clusters were rarely observed.

The P-domain is also actin rich and free of large organelles, with only a few MTs and intracellular membranes infiltrating the complex array of actin filaments (Fig. 2C, D). At the very front of the P-domain, the distinctive actin-rich sensory organelles – filopodia – are readily discriminated (Fig. 2D). We did not observe any examples of MTs infiltrating filopodia, consistent with previous findings that these are rare events (Schaefer et al., 2002). Filopodia-derived actin bundles persist into the middle of the P-domain where there is additional F-actin (Fig. 2C). Although polysomes remain less frequent than in the C-domain, ribosomes are observed throughout the P-

domain and filopodia - they are, however, excluded from and not obviously associated with the F-actin bundles themselves (Fig. 2C, D). Small vesicles of diameter <100 nm are observed in the P-domain and are associated with both bundled or non-bundled F-actin.

We used the segmentation analysis from all our tomograms to quantitatively assess the molecular distribution of cellular components within the different regions of the growth cone (Fig. 3A, B). Overall, the intracellular contents of the growth cones we analysed show a consistent distribution that reflects the aforementioned qualitative description and previous observations (Geraldo and Gordon-Weeks, 2009). There is a sharp drop of MT density from the C-domain through the T-zone into the P-domain, and this is the inverse of F-actin distribution, where diverse supramolecular arrays of F-actin dominate the growth cone periphery (Fig. 3A). Larger membrane-bound organelles are relatively common in the C-domain of the growth cones (Fig. 3B), including vesiculotubular ER networks (Fig. 3C), large vesicles (>100 nm diameter, Fig. 3D) and components of the endolysosomal system (Fig. 3E). In the P-domain, these cellular components are very rare and are perhaps excluded because of their physical dimensions. The distribution of smaller (<100 nm diameter) round or oblong vesicles is more variable among the different growth cones studied (Fig. 3F). While a variety of small vesicles were observed in the P-domain and even in filopodia, those with clathrin-coats were only observed in the C-domain (Fig. 3G). Ribosome distribution remains relatively constant throughout the growth cone, except in the filopodia where they are more abundant, especially compared to the rest of the P-domain (Fig. 3H).

Pseudo-crystalline organisation of neuronal filopodia actin bundles

To understand the integration of the F-actin and MT networks, we investigated the structure and organisation of these cytoskeleton components more closely. The molecular detail visible in our tomograms allowed us to characterise the diverse manifestations of the actin cytoskeleton that dominate the outer portions of the neuronal growth cone. At the very front of the growth cones, several filopodial regions are typically captured in each tomogram (Fig. 2D, 4A,). The dominant feature of filopodia are the tight bundles of F-actin filaments (Fig. 4B), which occupy the

majority of their volume. Surrounding the bundles, single or pairs of actin filaments lie beneath the membrane, some running roughly perpendicular to the filopodial axis (Fig 4A, B), and some of which directly feed into/out of the filopodial bundles themselves. Smaller filopodial extensions (less than ~ 400 nm diameter) contain a single F-actin bundle, while larger filopodia contain 2-3 individual bundles which exchange filaments or coalesce into larger bundles (Fig 4B, 2D). Other non-cortical, non-bundled actin is also found flanked by bundles, or between bundles and the membrane (Fig 4B, 2D).

Filaments within the bundles themselves are arranged in a characteristic 2D hexagonal, pseudo-crystalline array (Fig. 4B) (Kureishy et al., 2002). Although this arrangement is found in all the filopodia we observed, the hexagonal arrangement is not strictly maintained along an entire bundle length - the positions of individual filaments meander within the larger bundles, and overall bundle thickness also varies (Sup. Video 2). The filopodia bundles we observed are between 4 and 8 filaments in height and 9 and 14 filaments in width (Fig. 4C), with an inter-filament spacing of ~12 nm (Fig. 4D). Connecting density between adjacent filaments was spaced at ~37 nm intervals along the diagonals of the hexagonal array (Fig. 4E).

The characteristic hexagonal filament organisation of filopodia-derived bundles - in which the majority of filaments exhibit regular cross-links every ~37 nm (Fig. 4) - acts as a molecular signature to track their retrograde incorporation into the P-domain cytoplasm. Our data show how filopodia actin bundles penetrate and integrate into the complex actin-rich environment of the P-domain (Fig. 2C, 5A). The filament arrangement is very consistent between different bundles, both within the same filopodia, between different filopodia and in filopodia bundles that extend into the P-domain (Sup. Fig. 2). To better understand its molecular organisation, we performed sub-tomogram averaging of 341 volumes of 68 by 68 by 68 nm, encompassing a central 7-filament hexagonal repeating unit (Fig. 5B-D). In the resulting 3D reconstruction (with a nominal resolution of 29 Å, Sup. Fig. 3), individual 5.5 nm actin subunits are readily distinguished along each filament, all of which exhibit a half helical pitch distance of ~37 nm (Fig. 5C). Densities that crosslink the filaments are regularly spaced and connect both the central filament (labelled filament 0, Fig. 5B) with four of the six surrounding filaments (filaments 2,3,5,6, Fig. 5B-D; Sup. Video 3).

Density also connects the peripheral filament pairs 1-2, 3-4, 4-5 and 6-1 (Fig. 5B). The distribution of these links relates to the underlying helical structure of the individual actin filaments. When viewed as a 2D slice parallel to the filament axes, cross-links join filament 0 to filaments 2 and 5 every 37 nm and, orthogonally, filament 0 to filaments 3 and 6 (Fig. 5C, D). Cross-links therefore only occur where the outer edge of adjacent, helically aligned filaments come closest to each other (Fig. 5C, Fig. 4E). For this reason, the two cross-linked orthogonal planes (2-0-5 and 3-0-6) do not have their cross-links at the same position along the filament axis (Fig. 5D). Because there are no cross-links in the 1-0-4 plane, there is a repeating pattern of cross-links along the bundle axis, joining the central filament (0) to filaments 3 and 6 followed by a 12.3 nm gap, then connections to filaments 2 and 5, followed by a 24.6 nm gap to the next cross-links with filaments 3 and 6 (Fig. 5D, Sup. Video 3). This set of cross-links results in an approximate stoichiometry of 1 cross-linking density per ~5 actin monomers. Although the resolution of our data is not sufficient to determine whether every cross-link is composed of the same protein, based on previous *in vitro* and *in vivo* studies, these bundles are most likely to be built by fascin, which is known to localise to P-domain radial bundles and play a key role in filopodia structure (Cohan et al., 2001; Edwards and Bryan, 1995; Kureishy et al., 2002; Mosialos et al., 1994; Sasaki et al., 1996).

Modulation of F-actin arrays in growth cone P-domains

Despite the conservation of the core structure of the filopodial bundles, strikingly, a minority of filaments - either within the bundles, particularly at their periphery, or in separate filaments in the P-domain (Fig. 5E, Sup. Fig. 4A-C) - have a distinct appearance and a shorter half helical pitch length of ~27 nm (Fig. 5E,F). There is no evidence of filaments with intermediate half helical pitch length (Fig. 5F), and the ~27nm half pitch filaments tend to be shorter and lack regular cross-links to adjacent filaments (Fig. 5E, Sup. Fig. 4). Furthermore, these short-pitch filaments generally meander more within the bundle, and often appear to be breaking away from, or disrupting the regularity of, the bundle with which they are associated (Sup. Fig. 4A,B). Some individual filaments clearly transition from one helical half pitch length to the other (Sup. Fig. 4C).

Examples of both of the ~37 nm and ~27 nm half helical pitch filament populations were sufficiently plentiful that sub-tomogram averages of each could be calculated (Fig. 5G & Sup. Fig. 3). These reconstructions recapitulate the different actin twists and helical pitches visible in the tomogram 2D slices (Fig. 5G). In addition, the reconstruction of the ~27nm half helical pitch filaments provides evidence of additional binding protein(s) that are likely to be the origin of the shorter filament twist. Our dataset is not sufficiently large to allow further interrogation of whether there are different regulators bound to the filaments. However, based on extensive prior knowledge of a) the role of cofilin/ADF family members in regulating the actin cytoskeleton in migrating cells (Gungabissoon and Bamburg, 2003) and b) the known structural twist imposed by cofilin/ADF family members on F-actin filaments (Galkin et al., 2011; Galkin et al., 2001; Huehn et al., 2020; McGough et al., 1997; Tanaka et al., 2018), we rigid-body fitted F-actin-cofilin (PDB: 3JOS (Galkin et al., 2011) within this density (Fig. 5H, Sup. Video 4), which exhibited a very good match (0.87 model to map cross-correlation calculated in Chimera (Pettersen et al., 2004)). The binding site of cofilin - longitudinally between actin subunits along F-actin - corresponded well with the non-actin density in the reconstruction. Our ability to visualise this density in the sub-tomogram averages of these short-pitch actin filaments suggests high binding protein occupancy; such high occupancy, and the observation of extended stretches with a consistent ~27nm half helical pitch in the raw tomograms, is consistent with the reported cooperativity of cofilin binding *in vitro* (Huehn et al., 2018).

The P-domain also contained branched F-actin networks formed from a mixture of single filaments and small bundles between the filopodia-derived actin bundles (Fig. 5A). Filament branching was observed in this network, originating from the sides of single filaments and, less frequently, from F-actin bundles, all at ~70° angles (Fig. 5I) and consistent with Arp2/3 complex mediated branching. While the branched F-actin network is distributed throughout the P-domain, the branch points themselves are primarily located close to the dorsal and ventral membranes (Fig. 5J).

The mixed cytoskeletal economy of the T-zone

The T-zone cytoskeleton is characterised by two key features; the termination of radially organised F-actin bundles derived from the P-domain, and the termination of the majority of MTs originating from the C-domain. F-actin bundles organised like those seen in filopodia extend from the P-domain into the T-zone (Fig. 6A, yellow), oriented radially towards the front of the growth cone. These apparently filopodia-derived 3D bundles, although containing fewer filaments (maximum height of ~4 filaments, maximum width of 8 filaments), exhibit the characteristic average inter-filament spacing of 12 nm in a roughly hexagonal distribution, with individual filaments exhibiting ~37nm half helical pitch lengths (Fig. 6B,C). These bundles tend to taper within the T-zone, with sub-bundles and single filaments often bending off perpendicularly to the main bundle axis (Fig. 6A,D). However, even when filaments are only cross-linked in 1D, they are regularly spaced and connected by crosslinking density at ~37nm intervals (Fig. 6D,E). As was also observed in the P-domain, a minority of filaments, typically shorter and at the periphery of the bundles, exhibit a ~27 nm half helical pitch length (Fig. 6F). At least in snail growth cones, fascin concentrations decrease as radial bundles enter the T-zone (Cohan et al., 2001), and it is therefore possible that a different F-actin cross-linker operates in the T-zone to ensure that large hexagonal array bundles do not dominate organisation of the cytoskeleton outside the P-domain.

Compared to the P-domain, the radial actin bundles are less dense in the T-zone, where they terminate (Fig. 2B,C), and they are interspersed among smaller bundles which are orientated parallel to the growth cone circumference (Fig 6A & Fig 2B, orange features). Additionally, numerous individual filaments run parallel or perpendicular to the radial bundles (Fig. 6A, 2B, grey features). These distinct T-zone actin populations are often clearly derived from axial bundles themselves (Fig. 6A, D-G), although their overall organisation is looser and apparently less precisely organised, particularly at the cell membrane. Circumferentially organised F-actin also runs roughly perpendicular to the periphery-oriented MTs, but does not appear to block the MT trajectory - rather it lies on either side of these MTs (Fig. 6A, pink features). Branched actin arrays suggestive of Arp2/3 activity are also visible between the more ordered actin bundles and the T-zone membrane (Fig. 6H). Some individual non-bundled filaments exhibited a ~27nm half helical pitch length (Fig 6F, Sup. Fig. 4D). Thus, while tomograms of the growth cone T-zone show that the F-

actin network is overall less dense and less ordered than the P-domain, they also clearly demonstrate that the actin cytoskeleton is organised in distinct populations, mediated by the coordinated activities of regulatory proteins.

Growth cone microtubule architecture and interactions with F-actin

MTs are most prevalent in the C-domain, although they do not form ordered bundled arrays as is seen for F-actin in the growth cone periphery (Fig. 2A-C). All observed MTs throughout the growth cone exhibit a canonical 13-protofilament architecture (N=141 from 11 tomograms) according to analysis of both longitudinal moiré patterns and transverse segment rotational averages (Fig. 7A). Transverse segment rotational averages of these MTs exhibit a handedness that allows MT polarity determination, as described previously (Bouchet-Marquis et al., 2007; Sosa and Chretien, 1998). We could thereby show that the vast majority of growth cone MTs were orientated with their plus end direction towards the growth cone periphery, as found previously in murine axons (Baas and Lin, 2011), with only a few exceptions found in C-domain and T-zone (Fig. 7B) . A further subset of MTs in the T-zone and C-domain were either short, straight and perpendicular to the axonal axis (with both ends visible), or were long and looped ~180º such that they bent back on themselves, and thus neither of their ends were pointed towards the periphery (Fig. 7B (N/A subset), Fig. 2A & Fig. 6A).

The highest frequency of MT ends as a proportion of MT length was observed in the T-zone (Fig. 7C) and were mainly blunt-ended in appearance, although MTs with tapering ends were occasionally observed (Fig. 7D-F). Of the 6 tapered MT end tomograms, 4 were compatible with polarity determination, of which 3 were plus ends (2 in the axon and 1 in the C-domain) and 1 was a minus end (C-domain) (Fig. 7D, F). No examples of MTs with capped ends were observed, consistent with the absence of γ-tubulin ring complexes from growth cones (Stiess et al., 2010).

In both the T-zone and the P-domain (where MTs are rarer), densities were observed linking the sides of periphery-orientated MTs to parallel large axial F-actin bundles, both along their lattice and at their ends (Fig. 7G). In addition, smaller F-actin bundles orientated roughly perpendicular to these MTs were associated with

their dorsal and ventral surfaces (Fig. 7H). Cross-talk between MT and F-actin is vital for axon pathfinding, and our cryo-ET data provide evidence of a diversity of interactions that could mediate integration between the filament systems.

Lumenal particles and lattice defects in growth cone microtubules

The neuronal MTs in our tomograms frequently exhibited particles within their lumens, as has been previously described (Atherton et al., 2018; Foster et al., 2021; Garvalov et al., 2006). We refer to these here using the generic “lumenal particles”, rather than MT inner proteins (MIPs,) since in many cases we cannot visualise a direct association with the MT inner wall, a defining characteristic of MIPs (Nicastro et al., 2006) (Fig. 8A). The neuronal lumenal particles are not uniformly distributed in the growth cone (Fig. 8B); MTs in and adjacent to the axon and C-domain – where there is an overall greater density of MTs – generally exhibit more lumenal particles per tubulin dimer length (Fig. 8B), whereas these particles become increasingly sparse in MTs in the T-zone and P-domain. However, in some growth cone regions - particularly T-zones - there is a high degree of variability between different tomograms. Furthermore, within the same tomogram, neighbouring MTs - and even parts of the same MT (Fig. 8A) - exhibited different particle densities (Fig. 8C), with the most densely packed regions containing a particle roughly every 8nm. Particle frequency did not obviously differ between curved and straight MT regions or with proximity to MT ends (Fig. 2, Fig. 8C & Fig. 7E).

The particles themselves are not identical (Fig. 8A, D, E). While the mean lumenal particle diameter is 7.8 nm ± 1.7 (S.D.), the particles range from 3.9 to 14.7 nm, include ring-shaped structures with a diameter of 7-10 nm (Fig. 8D, white arrows) also described by (Foster et al., 2021), as well as smaller, more globular particles of 4-6 nm diameter (Fig. 8D, black arrows). The average size corresponds roughly to a molecular weight of ~ 200 kDa (with a range of 15 to ~1400 kDa, (Erickson, 2009). MAP6 has been shown to form ~9 nm diameter lumenal particles *in vitro* and in neurons (Cuveillier et al., 2020). While it is likely that MAP6 contributes to lumenal particles in our neuronal MTs, it is by no means the only protein involved. When MTs are viewed in cross-section, particles are not specifically localised within the lumenal space – some are located centrally while others appear to associate with the inner

surface of the MT lattice (Fig. 8D). Based on the volume of the MT lumen, the average volume of the particles and their average frequency, we estimate that they occupy roughly 7% of the total inner volume of neuronal MTs.

Further contributing to the complexity of the neuronal MT cytoskeleton, we observed numerous examples of defects and discontinuities in the cylindrical structure of the MT lattice, both in axonal regions and throughout the growth cone (Fig. 9A, B). Some of these discontinuities were very small, corresponding to a break of less than 2 dimers (16 nm) in length (Fig. 9B), whereas many were larger (Fig. 9A), with the largest being up to 600 nm long. The smallest observable defects did not appear to result from missing tubulin subunits, but rather subunits appeared to bend away from the MT axis, causing the lattice to incompletely close (Fig. 9B, blue boxed inset). Larger defects were often associated with curved MT regions (Fig. 9A), and thus were more prevalent in the growth cone than the axon (Fig. 9C). According to the analysis of MT moiré patterns, and transverse section rotational averages, no changes in protofilament number, MT architecture or polarity were observed on either side of defects (Fig. 9D), as can occur in *in vitro* polymerised MTs (Atherton et al., 2018; Chretien and Fuller, 2000; Chretien et al., 1992; Schaedel et al., 2019). Relative to MT length, tomograms of T-zones exhibited the most variable MT defect frequency, with two T-zone tomograms exhibiting an MT defect at least every 2.5 µm of MT length (Fig. 9E). The axon and C-domain exhibited the narrowest range of defect frequency, with a defect being observed every 20 µm on average (Fig. 9E). There was no obvious relationship between the frequency and/or size of defects and the density of the adjacent lumenal particles (Fig. 9A, B).

Cryo-ET of Dcx knockout neurons

DCX/Dcx is a modulator of neuronal growth cone morphology and the underlying MT and F-actin organisation (Bielas et al., 2007; Bott et al., 2020; Fu et al., 2013; Jean et al., 2012) and nucleates and stabilises 13-protofilament MTs *in vitro* (Moores et al., 2004). We therefore undertook cryo-ET of hippocampal neuron growth cones from Dcx knockout (KO) mice and analysed the detailed ultrastructural data, with a focus on the cytoskeleton (Fig. 10, Sup. Fig. 5, 6). Like WT neurons, Dcx KO neurons also exhibit classical stage 3 morphology after culture for 2-3 days *in vitro*

(Sup. Fig. 5A). By cryo-ET, the general organisation and appearance of the pre-cone axon and growth cone regions in the Dcx KO neurons are indistinguishable from those in WT neurons (Sup. Fig. 5 B-D & Sup. Fig. 5B). Specifically, F-actin ultrastructure and organisation resembles that in WT cells (Sup. Fig. 6A, B), with diverse actin arrays within the body of the growth cones and numerous protruding filopodia at their edges. Filopodial F-actin bundles appear indistinguishable from those in WT cells, and exhibit similar hexagonal stacking and crosslinking structures (Sup. Fig. 6B).

MTs in Dcx KO growth cones exhibit exclusively 13-protofilament architectures, as in WT neurons (Fig. 7A, 10A, Dcx KO, N=79 from 7 tomograms); sub-tomogram averages of both WT and Dcx MT segments are also consistent with a 13-protofilament architecture (Fig. 10B). Several tomograms of Dcx KO C-domains and pre-cone axons were suitable for MT polarity analysis (Fig. 10A). In the axons of Dcx KO neurons, MTs are exclusively oriented with their plus ends towards the growth cone as seen in WT neurons (Fig. 10C, 7B). A higher overall proportion of Dcx KO C-domain MTs are oriented with their minus ends towards the neuronal periphery than WT C-domain MTs (29% vs 10%), although this distribution was variable between tomograms (Fig. 10C). Lumenal particle frequency is similar in axons and the C-domain of WT and Dcx KO neurons (Fig. 10D).

MT ends are almost exclusively uncapped (with a possible single exception, Sup. Fig. 6D) in Dcx KO neurons. These MT ends are mainly blunt in appearance, although there appears to be a moderate increase in the proportion of tapered MT ends in the DCX knockout neurons (Fig. 10E, F compared with Fig. 7D). Importantly, however, a higher frequency of MT defects were observed in Dcx knockout C-domains (Mann-Whitney test, $p<0.05$) compared with WT C-domains (Fig. 10 G-H) with, in one C-domain tomogram a defect observed for every 1 µm of polymer length (Fig. 10H). Furthermore, a higher proportion of defects found in Dcx knockout growth cones are > 16nm (Fig. 10I).

DISCUSSION

We used cryo-ET to study neuronal growth cones and visualised the cytoskeletal machinery that makes essential contributions to growth cone function. Neural network-driven density segmentation and quantitative analysis of these rich data highlighted the distinct specialisations of the cytoskeleton in different parts of the growth cone, reflecting the complexity of its behaviour (Fig. 3).

The views of the actin cytoskeleton - which included the tightly structured actin bundles of the exploratory filopodia, the Arp2/3-mediated branched networks and the circumferential contractile actin bundles - emphasise the importance of the balance between different actin arrays in growth cone function, and provide molecular detail about how distinct populations are regulated and integrated. The regularity of the tightly bundled actin filaments that dominate the P-domain supported sub-tomogram averaging, revealing the 3D arrangement of regularly spaced cross-links that maintain bundle organisation (Fig. 5C, D). Different types of short F-actin cross-linkers, which our data cannot discriminate, will likely coexist in these bundles; however, bundle architecture is most consistent with the involvement of fascin (Ishikawa et al., 2003; Jansen et al., 2011; Kureishy et al., 2002; Winkelman et al., 2016; Yang et al., 2013), and similar to the hexagonal cross-linking model proposed from cryo-tomography studies of ‘neuronal-like’ cell lines (Aramaki et al., 2016). This is consistent with fascin’s known localisation in the growth cone P-domain, specifically to filopodia, and its known role in filopodia formation (Cohan et al., 2001; Sasaki et al., 1996). *In vitro* assembled fascin-mediated actin bundles with very similar overall architecture exhibit a maximum bundle size of ~20 filaments (Claessens et al., 2008), which is limited by bundle packing. However, we in primary neurons and others in a neuron-like cell line (Aramaki et al., 2016) observe examples of much bigger bundles (> 100 filaments) within filopodia. We also observe flexible actin filaments weaving between bundles which, together with other actin modulators, may loosen bundle packing sufficient to allow larger overall bundles. Larger but less stiff bundles may be important for the balance between the dynamic, exploratory activities of filopodia and the maintenance of their distinctive shape.

The distinctive organisation of the filopodia bundles allowed us to track their path into the P-domain and T-zone. Strikingly, we also observed lengths of shorter-pitch actin filaments emerging from these well-structured bundles, particularly in the P-domain. The ~27 nm half helical pitch length, wider appearance and 3D reconstruction of these emerging filaments suggest that cofilin is bound, consistent with its localisation to the P-domain and roles in filopodial F-actin severing and recycling (Bamburg and Bray, 1987; Breitsprecher et al., 2011; Gungabissoon and Bamburg, 2003; Marsick et al., 2010). *In vitro*, cofilin binds cooperatively to F-actin, alters the actin filament structure to produce a half helical pitch length of ~27 nm, and promotes ADP-actin filament severing (Bobkov et al., 2004; Galkin et al., 2001; Huehn et al., 2020; McCullough et al., 2008; McGough et al., 1997; Tanaka et al., 2018). When associated with bundles in our cryo-ET data, these short-pitch cofilin-like filaments were frequently peripheral, exhibited more positional fluidity within the bundle, and would often detach from the main filament cluster. They also did not appear to be regularly cross-linked to long-pitch filaments within bundles, likely due to the mismatch between the helical pitches of bundle filaments and those bound by cofilin. Our data provide good evidence that well-decorated cofilin-bound actin filaments exist in P-domain filopodial-derived bundles, and suggest that cofilin decoration may enable filament detachment from bundles before severing, thereby contributing to overall retrograde flow from the front of the cell (Vitriol et al., 2013).

Despite the cofilin-type activity in the P-domain, filopodia derived bundles gradually taper and terminate finally in the T-zone, often with F-actin bundles splitting apart and bending away into actin networks that run roughly perpendicular to filopodia bundles, also called actin arcs. Fascin localises to growth-cone radial filopodial bundles in all species examined (Edwards and Bryan, 1995; Mosialos et al., 1994; Sasaki et al., 1996); however, at least in the snail *Helisoma*, its concentration decreases into the T-zone (Cohan et al., 2001), so whether remaining crosslinks are fascin or another tight crosslinker is unclear. How filaments are bent away from F-actin bundles is also unclear; however myosin-II is known to unbundle F-actin, contribute to their severing and produce retrograde flow and bending forces in the T-zone (Burnette et al., 2008; Ishikawa et al., 2003; Medeiros et al., 2006; Schaefer et al., 2002). Further, since filament peeling is observed in both directions from filopodia-derived bundles, the resulting anti-parallel networks necessary for T-zone

myosin-II-mediated contractility can be formed. Cryo-EM images of myosin-II/F-actin complexes *in vitro* share striking similarities to the tapered unbundling observed here in T-zones *in situ* (Haviv et al., 2008). Drebrin is highly expressed in T-zones (Geraldo et al., 2008; Mizui et al., 2009) and competes with a number of tight F-actin cross-linking proteins including fascin (Ishikawa et al., 1994; Sasaki et al., 1996). As drebrin also stabilises F-actin (Mikati et al., 2013; Sharma et al., 2011), it could help to transform filopodial bundles to stable circumferential filaments in the T-zone contributing to actin-arc generation. While we did not observe F-actin stretches with the slightly increased half pitch associated with full drebrin occupancy (Mikati et al., 2013; Sharma et al., 2011), this may be because drebrin binds at sub-stoichiometric concentrations, or to very short stretches.

The C-domain is dominated by MTs that occasionally penetrate the T-zone but are rarely observed in the P-domain. In the T-zone, MTs encounter the diverse manifestations of the actin cytoskeleton, in particular the circumferential F-actin bundles that are moved centripetally by retrograde flow (Fig. 6A). The density of T-zone F-actin networks in our tomograms suggests that they do not create a physical barrier to MTs entering the P-domain. However, close association of MTs with both residual filopodial bundle and perpendicular F-actin is consistent with previously observed restriction of MT entry into the growth cone periphery primarily by retrograde flow (Burnette et al., 2008; Burnette et al., 2007; Kahn and Baas, 2016; Schaefer et al., 2002; Schaefer et al., 2008). Forces produced by retrograde flow have also been shown to bend and break growth cone MTs, which contributes to overall dynamics of growth cone MTs (Waterman-Storer and Salmon, 1997). Nevertheless, there is also abundant evidence in our data of MT-F-actin cross-linkers – both along the MT wall and at their ends - which likely mediate cytoskeleton cross-talk (Fig. 7G) (Chakraborty et al., 2020). In our tomograms, these were of sufficient diversity that more detailed structural investigation could not be undertaken. However, a number of end-binding proteins, MAPs and motors have been reported to form direct or indirect links to F-actin in growth cones, at least some of which are also important for neuronal migration (Cammarata et al., 2016; Geraldo and Gordon-Weeks, 2009; Kahn and Baas, 2016).

The MTs throughout the growth cone have a 13-protofilament architecture characteristic of many eukaryotic cells (Fig. 7A) (Tilney et al., 1973). In most cells, this uniform architecture is primarily mediated by the templating activity of γ-tubulin ring complexes (TuRCs) at MT organising centres (Kollman et al., 2011). Although γ-tubulin itself does not localise to the growth cone (Stiess et al., 2010), the uniformity of growth cone MT architecture could be because γ-tubulin nucleated 13-protofilament MTs are transported into the growth cone from the axon (Guha et al., 2021), because axon-derived 13-protofilament MTs are severed in the growth cone (Waterman-Storer and Salmon, 1997), and/or because other nucleation mechanisms exist specifically in the growth cone to maintain this protofilament architecture.

Growth cone MTs contain a diverse and unevenly distributed array of lumenal particles. Lumenal particle frequency varied dramatically between MTs, decreased towards the growth cone periphery and was particularly variable in T-zones. As MTs in the T-zone and beyond are much more dynamic compared to the axon and C-domains, MTs with high and low lumenal particle densities may represent populations of stable and dynamic MTs respectively; the more even distribution of lumenal particles in axon MTs would also be consistent with this idea (Foster et al., 2021). The identities of these lumenal particles in our tomograms remain unclear - some cytoplasmic components may simply be trapped during MT polymerisation. However, other densities are likely to be functionally relevant - for example, the neuronal MAP6 is likely to be among the neuronal components contributing to these particles in our dataset (Cuveillier et al., 2020). Enzymes responsible for post-translational modification – such as α-tubulin acetyltransferase (Roll-Mecak, 2020) – are also likely to be active in a subset of MTs. While individual G-actin subunits may be among the proteins located inside the MTs, we found no examples of F-actin (or other filaments) inside neuronal MTs, as was dramatically described in drug (kinesore)-treated HAP1 cells (Paul et al., 2020). Overall, the MT lumenal space remains an intriguing and poorly understood compartment within all cells.

A defining feature of MT organisation within axons is their uniform polarity with plus ends directed towards the cell periphery. This polarity was maintained in the majority of the growth cone MTs (Fig. 7B), consistent with the idea that at least a subset of

growth cone MTs originate in the axon. As well as maintaining axon compartment shape, the uniformity and stability of axonal MT polarity is particularly important for tightly regulated bidirectional transport to and from the growth cone (Koppers and Farias, 2021). In contrast, at least a subset of the MTs in the growth cone are dynamic (Baas and Black, 1990; Edson et al., 1993; Tanaka et al., 1995). Strikingly, however, the large majority of the imaged MT ends were relatively blunt, with a few exhibiting longer sheet-like extensions, but no evidence of extensively curled protofilaments that have been proposed to be the hallmark of both growing and shrinking MTs (McIntosh et al., 2018). The large number of MAPs found in neurons may constrain the morphologies of dynamic MT ends such that curling protofilaments are much less likely to form.

MT lattice defects, and the repair processes they promote, are increasingly understood to contribute to regulation of MT dynamics (Thery and Blanchoin, 2021). In our data, MTs in all parts of the growth cone exhibit discontinuities or substantial breaks in the MT lattice, particularly in the T-zone. Lumenal particle-forming MAP6 induces MT defects *in vitro* (Cuveillier et al., 2020); however, in our growth cone data there is no clear correlation between defects and lumenal particle density, and defects are more common in peripheral regions where there are overall fewer particles. We often observed large defects at points of MT curvature, and it therefore seems likely that at least some larger defects arise from strain-induced MT fraying, while short MTs may represent remnants of broken MTs caused by retrograde flow (Burnette et al., 2008; Schaefer et al., 2002; Schaefer et al., 2008; Waterman-Storer and Salmon, 1997).

DCX/Dcx has been linked to a number of roles in migrating neurons centred on its roles in cytoskeleton regulation (Bielas et al., 2007; Deuel et al., 2006; Friocourt et al., 2003; Fu et al., 2013; Jean et al., 2012; Li et al., 2021; Tint et al., 2009). In Dcx KO mouse hippocampal neurons, we observed that growth cone architecture and the overall organisation and distribution of the cytoskeleton components were comparable to WT neurons; this included F-actin organisation, even at the ultrastructural level, in contrast to an earlier report (Fu et al., 2013). *In vitro*, whereas MTs polymerised from diverse tubulin sources including mouse brain tubulin (Vemu et al., 2017) polymerise with a range of protofilament architectures (Ray et al., 1993),

DCX nucleates and selectively stabilises 13-protofilament architectures (Moores et al., 2004). In the Dcx KO growth cones, however, all MTs exhibited a 13-protofilament architecture, highlighting the role of diverse cellular factors in addition to Dcx in ensuring uniformity of MT architecture even in the absence of γ-TuRCs in the growth cone. However, in our Dcx KO tomograms, C-domain MTs exhibited a higher proportion of minus end out MTs, a higher frequency of defects, and a higher proportion of large compared to small defects. DCX/Dcx is highly expressed in growth cones where it has been shown to stabilise and straighten MTs (Jean et al., 2012; Tint et al., 2009) and its binding is modulated by MT curvature (Bechstedt et al., 2014; Ettinger et al., 2016). Taken together with our data, this suggests that absence of Dcx may lead to a higher frequency of curvature-induced MT fraying or breakage in C-domains, where Dcx is particularly abundant (Fig. 1B), and greater persistence of MT defects overall.

How might this potential role for DCX/Dcx explain brain developmental phenotypes caused by its absence? Immature neurons experience substantial compression forces during navigation of the densely packed layers of the developing brain (Tyler, 2012), and the requirement to maintain and repair ruptured MTs during migration may be particularly acute. The greater phenotypic severity caused by DCX absence in humans compared to mouse may reflect the greater complexity of this migration process during human brain development (Sun and Hevner, 2014). Cryo-ET will continue to be a vital tool for the molecular visualisation and dissection of machinery involved in key cellular processes including responses to guidance signals and injury in neurons. Insights arising from such studies will also inform developments of new treatments for neuronal damage and degeneration (Griffin and Bradke, 2020).

MATERIALS AND METHODS

Transgenic mice and genotyping

WT and Dcx KO mice were maintained on the Sv129Pas background with more than ten generations of backcrosses (Kappeler et al., 2007; Kappeler et al., 2006). Genotyping was performed by PCR to verify the inactivation of the Dcx gene in KO animals (Kappeler et al., 2006). All experiments were performed in accordance with institutional, national and international guidelines (EC directive 2010/63/UE) and were approved by the local ethical committees (French MESR N°: 00984_02). The day of confirmation of vaginal plug was defined as embryonic day zero (E0.5).

Neuronal cell dissociation and isolation

Embryonic mouse hippocampus was dissected at E17.5 in ice-cold 0.02 M HEPES in Ca^{2+}/Mg^{2+}-free HBSS (Gibco) and primary cell suspensions dissociated via incubation with 2.5 mg/ml trypsin (Sigma). After centrifugation to a pellet (5 min, 300g), cells were resuspended in culture media for light or electron microscopy experiments as indicated below.

Cell culture for fluorescence microscopy

For fluorescence microscopy experiments dissociated neuronal pellets were resuspended and cultured in Neurobasal medium supplemented with B27 (1%, Gibco), GlutaMAX (2 mM, Gibco), penicillin (100 units/ml, Invitrogen) and streptomycin (100 mg/ml, Invitrogen). Only mouse litters comprised of at least 1 WT and 1 Dcx KO animal were used. Dissociated cells were plated on 14 mm-diameter coverslips (0.3×10^5 cells/ coverslip) coated with poly-L-lysine (0.05 mg/ml, Sigma) and laminin (0.01 mg/ml, Invitrogen) and cultured at 37°C in the presence of 5% CO_2.

Fluorescence microscopy

Neurons were fixed after 3 days in vitro (DIV) following the protocol from (Tint et al., 2009), applying PEM buffer with 0.3% gluteraldehyde, 0.1% IgepalCA630, and 10 µM taxol for 10 min R.T. Coverslips were then washed 5X with PBS, 1X 15 min in PBS with 0.5% triton, 2X 7 min with 10 mg/mL sodium borohydride in PBS, and 5X with PBS. Neurons on coverslips were incubated with blocking solution (5% normal

goat serum, 0.1% Triton X-100 in 1X PBS) for 1 h at room temperature (RT), followed by incubation with primary antibodies for Dcx (Francis et al., 1999) and neuron-specific β3-tubulin (TUJ1, RD Biosystems) in blocking solution for 2 h at R.T. or overnight at 4°C. Secondary antibodies (Invitrogen) were incubated in blocking solution combined with Hoechst for 60 min at RT in the dark, followed by 60 min incubation with phalloidin-A633 (Invitrogen) in PBS. Coverslips were mounted with Fluoromount G (Southern Biotechnology).

Neuronal cell culture and preparation for cryo-EM

For electron microscopy experiments dissociated neuronal pellets were resuspended in Hibernate-E medium (Gibco) supplemented with B27 (Invitrogen) and Pen-Strep (100 units/ml penicillin and 100 mg/ml streptomycin, Invitrogen) and shipped overnight from Paris to London in the dark at 4°C in Hibernate-E media. Quantifoil R2/4 gold G200F1 Finder EM grids were placed on the surface of plastic culture dishes and sterilized under UV light. The dishes and overlaid EM grids were then coated with poly-d-lysine (Millipore) and mouse laminin (Thermofisher). Within 24–30 h of initial dissociation neurons were pelleted by centrifugation (5 min, 300g), then resuspended and plated in Neurobasal medium with B27 and Pen-Strep and cultured at 37°C in the presence of 5% CO_2 for 2–3 d *in vitro* without media change. Grids were extracted from culture dishes, 3 µl of conditioned culture media added, blotted for 8-10s and plunge-vitrified in liquid ethane using a Vitrobot (FEI) set at 37°C and 80% humidity.

Cryo-ET data collection

Cryo-electron tomography was performed using a Tecnai G2 Polara operating at 300kV with a Quantum post-column energy filter (Gatan), in zero-loss imaging mode with a 20 eV energy-selecting slit. Single-axis cryo-electron tomography was performed at 3-6 µm defocus with a K2 Summit direct electron detector (Gatan) operating in counting mode (at 5 e- per pixel per second) with a final sampling of 5.38 Å per pixel. Dose-symmetric tilt-series (Hagen et al., 2017) within a -60° to +60° tilt range were collected at 3° increments to give a total dose of 110 e-/$Å^2$. Movies of three or four subframes per second were collected at each tilt and aligned on-the-fly using MotionCor2 (Zheng et al., 2017).

Cryo-ET image processing

Fiducial-less alignment via patch-tracking was performed on each tilt series in the Etomo graphical user interface to IMOD v.4.9.0 (Kremer et al., 1996). CTF was determined at each tilt using CTFFIND4 (Rohou and Grigorieff, 2015) and then a dose-weighted aligned tilt-series was produced using Summovie (Grant and Grigorieff, 2015) under the control of custom scripts. Three-dimensional CTF correction and tomogram reconstruction was performed by weighted back-projection of dose-weighted tilt series with novaCTF (Turonova et al., 2017) using custom scripts.

Semi-automated tomogram segmentation was performed using the tomoseg module of EMAN2 v.2.2 (Chen et al., 2017). 4x binned tomograms with low frequencies amplified via a positive B-factor of 100,000 were used for training and segmentation purposes. Segmentations were further cleaned manually in Chimera (Pettersen et al., 2004) for display, via a combination of masking, ‘volume eraser’ and ‘hide dust’ tools.

Subtomogram averaging of MT and F-actin filaments was performed in Dynamo. Particle coordinates were picked from 4x binned tomograms using filament model tools. Initial 40 Å low-pass filtered references were generated from data aligned only along filament axes. Initial coarse alignment was performed using 4x binned data, before finer alignment with 1x binned data.

ACKNOWLEDGEMENTS

MAS and FF were associated with the BioPsy Labex project and the Ecole des Neurosciences de Paris Ile-de-France (ENP) network. We are particularly grateful to the IFM animal experimentation platform for mouse maintenance and production (supported by Inserm, the Région Ile de France and the Fondation Bettencourt Schueller). We thank Natasha Lukoyanova for support during cryo-EM data collection, and Joshua Hutchings, Joseph Beton and Phillip Gordon-Weeks for useful discussions and technical advice.

COMPETING INTERESTS

No competing interests declared.

FUNDING

J.A. was supported by a grant from the Medical Research Council (MRC), U.K. (MR/R000352/1) to C.A.M. Cryo-EM data were collected on equipment funded by the Wellcome Trust, U.K. (079605/Z/06/Z) and the Biotechnology and Biological Sciences Research Council (BBSRC) UK (BB/L014211/1). FF's salary and institute were supported by Inserm, CNRS and Sorbonne University. FF's group was particularly supported by the following funding ANR-16-CE16-0011-03 and EU-HEALTH-2013, DESIRE, N° 60253 (also funding MAS's salary) and the European Cooperation on Science and Technology (COST Action CA16118).

AUTHOR CONTRIBUTIONS

J.A.: conceptualization, methodology, formal analysis, investigation, writing – original draft preparation, visualization;

M.S.: investigation, methodology, writing – review and editing, visualization;

F.F.: conceptualization, resources, writing – review and editing, supervision, project administration, funding acquisition;

C.A.M.: conceptualization, writing – original draft preparation, supervision, project administration, funding acquisition.

FIGURE LEGENDS

Figure 1. Cryo-electron tomography of primary neuronal growth cones.
(A) Mouse primary hippocampal neuron cultured for 3 days *in vitro*, demonstrating the characteristic polarised stage 3 morphology, labelled as indicated with DAPI (nucleus) and phalloidin (F-actin) dyes and antibodies to β3-tubulin and Dcx; **(B)** Fluorescence light microscopy images of a mouse hippocampal neuron growth cone labelled as indicated with phalloidin (F-actin) dye and antibodies to β3-tubulin and Dcx; the central domain (C), transition zone (T) and peripheral domain (P) are indicated on the composite image. **(C)** Low magnification cryo-EM image of a growth cone. The cell membrane is depicted in blue; the C-domain (C), transition zone (T) and peripheral domain (P) are indicated; F, filopodia; L, Lamellipodia; H, underlying holes in the carbon substrate; I, Ice contamination; a representative region for tilt series data collection is indicated by the dashed cyan boxed region; **(D)** Higher magnification view of a slice through the tomogram corresponding to the boxed region in (C), binned by 4, with MTs false coloured in magenta; AB, actin bundles; edges of the carbon substrate hole are indicated with black arrows. Scale bars: (A) = 20 µm, (B) = 10 µm, (C) = 2 µm, (D) = 250 nm.

Figure 2. The molecular landscape of neuronal growth cones.
Example tomograms and corresponding segmentations from different growth cone regions; **(A)** C-domain, **(B)** T-zone, **(C)** P-domain, **(D)** P-domain filopodia. Left panels show central sections through binned x 4 tomograms, with MTs (magenta) and outer membrane (blue) indicated with overlaid false colouring. Direction of the leading-edge distal periphery is indicated with large black arrows containing a ‘P’ and edges of the carbon substrate hole are indicated with small black arrows. Middle panels show corresponding whole volume 3D semi-automated segmentations. Right panels show transverse sections of the segmented regions indicated with dashed lines in corresponding central panels (section viewing direction also indicated in central panels). Segmentation colouring is according to the key. Scale bars = 200 nm.

Figure 3. Quantitative analysis of growth cone component distribution.

A) Relative segmentation volumes of MTs and F-actin in different growth cone regions. **B)** Relative segmentation volume of large vesicles and organelles (including mitochondria), in different growth cone regions. **C)** Smooth vesiculotubular ER of the C-domain, arranged as sacs and thin connecting tubes, false coloured in semi-transparent cyan. Scale bar = 100 nm. **D)** Large vesicles over 100 nm diameter in the C-domain and T-zone, false coloured in semi-transparent cyan. Arrowheads indicate embedded protein coats. Scale bar = 60 nm. **E)** Components of the endolysosomal system in the C-domain (left, early/sorting endosome, right, late endosome/multi-vesicular body), false coloured in semi-transparent green. Arrow indicates inward budding site. Scale bar = 60 nm. **F)** Relative segmentation volume of large vesicles and organelles (including mitochondria), in different growth cone regions. **G)** Small vesicles under 100 nm diameter in indicated growth cone regions, false coloured in semi-transparent purple. Examples of clathrin coats are false coloured in orange. Scale bar = 60 nm. **H)** Relative segmentation volume of ribosomes, in different growth cone regions. Panels C-E and G show longitudinal views in 4 x binned tomograms. For panels A, B and F, absolute segmentation volumes for MTs, F-actin, large vesicles and organelles (including mitochondria), small vesicles (<100 nm diameter) and ribosomes were measured in Chimera (Pettersen et al., 2004). Relative segmentation volume for each feature indicated is expressed as a % of the total volume of all these features combined. Axon, n = 2, C-domain, n = 3, T-zone, n = 3, P-domain, n = 2, P-domain filopodia, n = 2, dashed lines indicate the S.D.

Figure 4. Ultrastructure of the ordered filopodial F-actin arrays.

(A) Central section through a tomogram (binned x4), left, and semi-automated segmented segmentation (right) of 2 adjacent filopodia. Black arrows indicate F-actin filaments that connect adjacent F-actin bundles; black arrowheads indicate where two F-actin bundles merge to form a larger bundle. Direction of the very front of the cell is indicated with a large black arrow containing a ‘P,’ while edges of the carbon substrate hole are indicated with black arrows. False colouring is according to the key. **(B)** Sections through a binned x 4 tomogram of a single large filopodium showing the (i) longitudinal central region, (ii) the dorsal cortex and (iii) a transverse cross-section (~20 nm depth). Cyan dashed lines indicate the relationship of the panel views to one another as indicated. A single hexagonal F-actin bundle unit as

referred to in panel D is indicated within a dashed red hexagon. **(C)** Super-plot (Lord et al., 2020) quantification of maximum width and height of filopodial bundles in number of filaments. Each data point represents an individual filopodial F-actin bundle (N=14 from 4 tomograms, shown as different colours), with a line indicating the overall median. Mean values for each tomogram are shown in their respective colours with different larger shapes. Overall mean width, 11.6 ± 1.7 S.D, mean height 6.4 ± 1.2 S.D filaments. **(D)** Left; transverse view through a filopodial F-actin bundle (~20 nm depth), showing its characteristic hexagonal arrangement. Exemplar inter-filament distances are shown as yellow dashed lines. Right; Super-plot (Lord et al., 2020) of inter-filament distances in filopodial F-actin bundles. Each data point represents a separate adjacent filament pair (N=60 from 4 tomograms, shown as different colours). Mean values for each tomogram are shown in their respective colours with different larger shapes. Line indicates the overall mean (12.1 nm ± 1.2 S.D). **(E)** Left, a single cross-linked sheet in a filopodial bundle (4 x binned tomogram), showing ~37 nm longitudinal cross-link separation, indicated with arrows and dashed lines; right, super-plot (Lord et al., 2020) quantification of regular longitudinal crosslink separation distance in P-domain filopodial F-actin bundles. Each data point represents an individual pair of adjacent cross-links along the F-actin longitudinal axis (N=44 from 4 tomograms, shown as different colours). Mean values for each tomogram are shown in their respective colours with different larger shapes. Line indicates the overall mean (37.1 nm ± 1.9 S.D). Scale bars: A = 200 nm, B = 100 nm, D = 10 nm.

Figure 5: Complexity and modulation of F-actin arrays in growth cone P-domains

(A) Central section through a tomogram (binned x4), left, and semi-automated segmented rendering (right) of a P-domain region. L= Lamellipodial branched F-actin network; black arrowheads indicate branched cortical F-actin networks running over the surface of the F-actin bundles. Direction of the leading-edge distal periphery indicated with a large black arrow containing a ‘P’ while edges of the carbon substrate hole are indicated with black arrows. False colouring is according to the key. **(B-D)** 3D subtomogram average (yellow mesh) calculated from hexagonal arrays of P-domain bundles. Panel B shows a transverse section with filaments numbered to aid description (central filament 0, surrounding filaments 1-6) and

indicating 90º rotated viewpoints shown in panels C and D. Individual cross-links are labelled according to the filament numbers they connect. **(C)** 37 nm separation of cross-links along single 2D plane connecting 2-0-5 filaments. **(D)** Cross-linking superstructure showing cross-links that connect both 2-0-5 and 3-0-6 filaments. Individual cross-links are labelled as in panel B. **(E**) i) Longitudinal and ii) transverse (~20 nm depth) views of a large F-actin bundle in a 2x binned P-domain tomogram. Dashed cyan line in i) illustrates position of transverse section in ii). Examples of common canonical ~37 nm F-actin half helical pitch lengths are indicated with yellow dashed arrows, while shorter, rarer ~27 nm F-actin half helical pitch lengths are shown with green dashed arrows. A short-pitch filament length is false coloured in green and additionally indicated in ii) with a green arrowhead. **(F)** Super-plot quantification (Lord et al., 2020) of F-actin longitudinal half helical pitch lengths in P-domain long and short-pitch F-actin. Individual points indicate single measurements along a filament axis, while colours indicate different filaments. Mean values for each filament are shown in their respective colours with different larger shapes. Individual lines indicate overall median values. Long-pitch filaments; mean = 37.2 nm ± 2.4 S.D, N=32 from 4 filaments (from 3 tomograms); short-pitch filaments; mean = 27.3 nm ± 1.6 S.D, N=30 4 filaments from 3 tomograms). **(G)** Projections through 3D subtomogram averages of long-pitch (left) and short-pitch (right) filaments to show filament half pitch distances, as indicated in yellow and green respectively. Long-pitch filament=average of 1461 volumes. Short-pitch filament = average of 621 volumes. Volumes were low-pass filtered to their estimated resolutions at the Fourier Shell Correlation (FSC) 0.5 criterion (Sup. Fig. 3). **(H)** 3D subtomogram averages of long-pitch filaments (left, mesh density) and short-pitch (right, mesh density) filaments with fitted F-actin (PDB: 7BT7, (Kumari et al., 2020) or F-actin-cofilin (PDB: 3JOS, (Galkin et al., 2011)) atomic models respectively. F-Actin and cofilin atomic models are coloured in grey and green respectively with mesh density coloured to match within 10 Å of the underlying atomic models. **(I)** P-domain 4 x binned tomogram sections illustrating F-actin branching off F-actin bundles (top left) or single filaments (bottom left). Exemplar F-actin branches and branching angles are indicated with cyan false colouring. Right; Super-plot (Lord et al., 2020) of P-domain branching angles. Each data point represents an individual branching structure (N=12 from 3 tomograms, shown as different colours). Mean values for each tomogram are shown in their respective colours with different larger shapes. Line

indicates the overall mean (70.1º ± 2.6 S.D). **(J)** Longitudinal sections of a 2 x binned P-domain tomogram through left, a central region showing radial F-actin bundles in false yellow colour and right, the corresponding overlying cortical region, showing a F-actin branching points at the cell cortex. Branching points are indicated with cyan arrows. Scale bars: A = 200 nm, I = 40 nm, J = 50 nm.

Figure 6: Diverse F-actin arrays in neuronal growth cone T-zone

(A) Central section through a tomogram (binned x4), left, and semi-automated segmented rendering (right) of a T-zone region. Direction of the leading-edge distal periphery indicated with a large black arrow containing a 'P' while edges of the carbon substrate hole are indicated with smaller black arrows. Segmentation false colouring is according to the key. **(B)** Transverse section through a radial F-actin bundle in a 4 x binned T-zone tomogram, showing hexagonal filament organisation as in the P-domain. Exemplar ~12 nm inter-filament distances are shown with yellow dashed lines. **(C)** Longitudinal section through a radial F-actin hexagonal bundle in a 2 x binned T-zone tomogram, showing 37 nm half helical pitch lengths similar to that observed in P-domain bundles, indicated by arrows. **(D)** Longitudinal section through a 4 x binned tomogram of a radial F-actin bundle taper and a derived circumferential F-actin bundle, with white arrows indicating F-actin cross-links. Blue arrows indicate points where filaments bend-off tapering radial F-actin bundles. White arrows indicate 37 nm inter-crosslink spacing along the filament axis. **(E)** Longitudinal (left) and transverse (centre, ~20 nm depth) sections as indicated with red dashed lines of a tapering radial F-actin bundle in a 4 x binned T-zone tomogram. A traced representation is included (right) to illustrate bundle tapering. White arrows indicating F-actin cross-links. Blue arrows indicate points where filaments bend-off the tapering radial F-actin bundle. White arrows indicate 37 nm inter-crosslink spacing along the filament axis. **(F)** i) Longitudinal and ii) transverse views of a tapering radial F-actin bundle in a 2 x binned T-zone tomogram. In i) distal and proximal are at the top and bottom of the image respectively. Dashed cyan line in i) indicates the position of transverse section in ii). Examples of ~37 nm F-actin half helical pitch lengths are indicated with yellow dashed arrows, while ~27 nm F-actin half helical pitch lengths are shown with green dashed arrows. Short-pitch filament lengths are false-coloured in green and their transverse positions within the bundle are additionally indicated in ii) with a green arrowhead. **(G)** Longitudinal sections of a radial F-actin bundle taper

(left) and an F-actin bundle-derived dislocated single filament (right) in a 2 x binned tomogram with dashed arrows indicating long F-actin half helical pitch lengths. **(H)** Longitudinal sections of a 2 x binned T-zone tomogram through left, a central region showing radial and circumferential F-actin bundles in false yellow and orange colour respectively and right, the corresponding overlying cortical region, showing F-actin branching points at the cell cortex. Branching points are illustrated with cyan arrows. Scale bars: A = 200 nm, D-E = 50 nm, F-H = 40 nm.

Figure 7: Organisation and architectures of microtubules within growth cones. **(A)** Analysis of exemplar MTs from different regions of growth cones and pre-cone axons to determine protofilament number and polarity. Each set of 3 images includes a ~30 nm thick longitudinal section through a 2 x binned MT volume (left) with its corresponding image Fourier filtered at the origin (right in red box) to better show 13-protofilament moiré patterns. Below is a corresponding MT rotational average of a 30 nm thick transverse section when viewed towards the cell periphery (as indicated with a large black arrow containing a ‘P’), which allows protofilament number to be counted and shows protofilament handedness (with a curved red arrow). According to the method of polarity determination using protofilament chirality, when viewed from the minus end or plus end, rotational average images exhibit clockwise or anticlockwise slew respectively (Bouchet-Marquis et al., 2007; Sosa and Chretien, 1998). In longitudinal sections the growth cone periphery is towards the top of the images, plus and minus end directions are indicated with a red ‘+’ and ‘–’ respectively, and the consensus protofilament (pf) architecture is indicated between dashed red lines. **(B)** MT polarity relative to the neuron periphery was quantified in individual tomograms of axons and different growth cone regions. MTs assigned ‘n/a’ were either perpendicular to the axon axis or were bent ~180º such that both minus and plus directions were orientated outwards. Axon N=59 total plus-end peripheral MTs, 0 minus-end peripheral from 3 tomograms (each from a different cell); C-domain N=69 total plus-end peripheral MTs, 6 minus-end peripheral, 2 n/a from 4 tomograms (each from a different cell); T-zone N=7 total plus-end peripheral MTs, 3 minus-end peripheral, 1 n/a from 3 tomograms (each from a different cell), P-domain (PD) N=2 total plus-end peripheral MTs, 0 minus-end peripheral, 0 n/a from 1 tomogram. **(C)** Quantification of the frequency of MT ends per 1 µm MT length in individual tomograms of axons and different growth cone regions. Each data point

represents a separate tomogram; axon=4, C-domain=7, T-zone=4, P-domain=1. Line indicates the mean from all tomograms for each region. 50 MT ends were found in a total of 318 µm MT length analysed. **(D)** Quantification of the absolute number of blunt and tapered ends found in individual tomograms of axons and different growth cone regions (number of tomograms of axon=4, C-domain=7 (one tomogram contained no ends), T-zone=4, P-domain=1). **(E)** Longitudinal views of blunt and tapered **(F)** MT ends in the axon and different growth cone regions as labelled. Blunt ends are shown as 10 nm thick slices through 4x binned tomograms, while tapered ends are shown as 30 nm thick slices through 2x binned tomograms. MTs and taper lengths are false coloured in semi-transparent magenta and orange respectively. A traced representation of each tapered MT end is shown to its right for clarity. Plus and minus ends are indicated on images with a red '+' and '–' respectively. **(G)** Four longitudinal sections through regions of a single MT associated in parallel with P-domain F-actin bundles. Black and white arrows indicate cross-links between the MT shaft or MT tip and F-actin bundles respectively, and cyan indicates membranous ER. **(H)** Two 3D sections (left and right) through T-zone segmentations, with black arrows indicating transverse F-actin bundles running perpendicular on dorsal and ventral surfaces of periphery-orientated MTs. Segmentation colouring is as in Fig. 6A. Scale bars: E-G = 50 nm, H = 100 nm.

Figure 8: Lumenal particles in neuronal growth cone MTs.

(A) Longitudinal views of MTs in 2 x binned tomograms showing different types and frequencies of lumenal particles. Orange dashed boxed regions indicate regions where particles are found every ~8nm. White arrows show larger ring-like particles ~7-10 nm in diameter, black arrows show smaller particles ~3-5 nm in diameter. **(B)** Super-plot (Lord et al., 2020) quantification of the frequency of lumenal particles per 8 nm MT length (a tubulin dimer) in the pre-cone axon and different growth cone domains. Each small data point represents a separate MT coloured by tomogram, mean frequency for individual tomograms are indicated with large coloured shapes, while lines indicate the overall medians. Overall means are as follows: Axon, mean = 0.43 ± 0.07 S.D, N = 94 MTs from 4 tomograms; C-domain, mean = 0.38 nm ± 0.09 S.D, N = 134 MTs from 7 tomograms; T-zone, mean = 0.26 ± 0.16 S.D, N = 22 MTs from 4 tomograms; P-domain, mean=0.19 ± 0.02 S.D, N=2 MTs from 1 tomogram).

(C) 3D segmentations of exemplar MTs (semi-transparent magenta) and lumenal particles (black) from the C-domain illustrating particle frequency variability. **(D)** An MT as in panel A, but with transverse sections (~5 nm depth) presented at positions indicated by the dashed coloured lines. White arrows again show larger ring-like particles ~7-10 nm in diameter, black arrows show smaller particles ~3-5 nm in diameter. **(E)** Super-plot (Lord et al., 2020) quantification of lumenal particle diameters by growth cone region. Each small data point represents a separate lumenal particle coloured by tomogram. Different small data point shapes indicate different MTs within each tomogram. Large coloured shapes indicate mean particle diameters within individual tomograms, while the lines indicate the overall medians. Overall means are as follows: Axon, mean = 7.6 nm ± 1.7 S.D, N = 122 from 4 tomograms; C-domain, mean = 7.9 nm ± 1.7 S.D, N = 217 from 7 tomograms; T-zone, mean = 7.9 ± 1.6 S.D, N = 97 from 4 tomograms; P-domain, mean = 8.0 ± 1.3 S.D, N = 21 from 1 tomogram. Scale bars: A, D = 50nm; C = 100 nm.

Figure 9: Lattice defects and discontinuities in neuronal growth cone MTs. **(A)** Longitudinal views of large (> 16 nm long) and **(B)** small (< 16 nm long) MT lattice defects in growth cones. Large and small lattice defects are shown as 30 nm thick slices through 2 x binned and 10 nm thick slices through 4x binned tomograms respectively. MTs and defect lengths are false coloured in semi-transparent magenta and orange respectively. A traced representation of each MT is shown alongside for clarity. Blue boxed insert in panel B is a 2 x binned (5 nm thick) version of the blue dashed boxed region above, with magenta and orange arrows pointing to tubulin monomers in the MT lattice and defect respectively. **(C)** Quantification of the absolute number of small (< 16 nm long) and large (> 16 nm long) defects found in the pre-cone axon and different growth cone domains (number of tomograms of axon = 4, C-domain = 7, T-zone = 4, P-domain = 1). **(D)** The centre panel shows a raw ~30 nm thick longitudinal slice of an MT including an MT defect (orange arrowhead). Right panels show Fourier filtered (at the origin, FF) images of the blue dashed boxed regions in the centre panel to reveal characteristic 13-protofilament moiré patterns either side of the defect. Left panels show raw and corresponding rotational average (RAv) images of a ~10 nm thick transverse section through the MT as indicated with a blue cyan dashed line, indicating 13 protofilaments in both cases. **(E)** Quantification of the frequency of defects per 1 µm MT length in the axon

and different growth cone domains. Each data point represents a separate tomogram; axon = 4, C-domain = 7, T-zone = 4, P-domain = 1. Scale bars: A, B, D=50 nm.

Figure 10: Evidence for increased microtubule defects in doublecortin knock-out neuronal growth cones.

(A) Analysis of example MTs from Dcx KO pre-cone axons and C-domains to determine protofilament number and polarity. Images and processing are as described for Fig 7A. **(B)** Transverse views (slightly tilted and viewed from the plus end) of sub-tomogram averages of a random subset of MTs in WT (left, 1200 MT segments taken from 13 MTs) and Dcx KO (right, 1190 MT segments taken from 20 MTs) neurons. The MT sub-tomogram averages are built from 13 protofilaments as indicated. Volumes were low-pass filtered to their estimated resolutions at the Fourier Shell Correlation (FSC) 0.5 criterion (Sup. Fig. 6C). **(C)** Using the transverse chirality method shown in panel A), MT polarity relative to the neuron periphery was quantified in individual tomograms of different growth cone regions. MTs given 'n/a' polarity were either perpendicular to the axon axis or were bent ~180º such that both minus and plus directions were orientated peripherally. Axon = 45 plus-end peripheral MTs, 0 minus-end peripheral from 3 tomograms (each from a different axon), C-domain = 23 plus-end peripheral MTs, 10 minus-end peripheral, 1 n/a from 3 tomograms (each from a different axon). **(D)** Super-plot (Lord et al., 2020) quantification of the frequency of lumenal particles per 8 nm MT length (a tubulin dimer) in the axon and C-domains of WT and Dcx KO neurons. Each small data point represents a separate MT coloured by tomogram, mean frequency for individual tomograms are indicated with large coloured shapes, while lines indicate the overall medians. Overall means are as follows: WT axon, mean = 0.43 ± 0.07 S.D, N = 94 MTs from 4 tomograms; C-domain, mean = 0.38 nm ± 0.09 S.D, N = 134 MTs from 7 tomograms. Dcx KO axon, mean = 0.43 ± 0.06 S.D, N = 78 MTs from 4 tomograms; Dcx KO C-domain, mean = 0.37 nm ± 0.07 S.D, N = 84 MTs from 5 tomograms. **(E)** Longitudinal views in 4 x binned tomograms of blunt and tapered MT plus and minus ends in Dcx KO growth cones. **(F)** Quantification of absolute numbers of blunt, tapered and capped MT ends in Dcx KO pre-cone axons and C-domains. Dataset size is the total number of individual MTs in multiple tomograms (5 Dcx KO axon tomograms, of which 2 had no ends, and 4 Dcx KO C-domain

tomograms). **(G)** Longitudinal views in 4 x binned tomograms of example MT defects in Dcx KO growth cones.**(H)** Quantification of the frequency of defects per 1 µm MT length in the pre-cone axon and C-domain regions of WT and Dcx KO neurons. Each data point represents a separate tomogram; WT axon = 4, WT C-domain = 7, Dcx KO axon = 3, Dcx KO C-domain = 4. Mann-Whitney tests; WT C-domain vs Dcx KO C-domain, $p < 0.05$ (*), WT axon vs Dcx KO axon, $p = 0.89$ (not significant). **(I)** Quantification of large and small MT lattice defects as a percentage of total MT lattice defects in WT (left) and Dcx KO (right) pre-cone axons and C-domains. Dataset sizes indicate the total number of defects. Panels E & G: MTs and lattice defects are false coloured in semi-transparent magenta and orange respectively. A traced representation of each MT is shown to its right for clarity. Scale bars: E and G = 50 nm.

REFERENCES

Aramaki, S., K. Mayanagi, M. Jin, K. Aoyama, and T. Yasunaga. 2016. Filopodia formation by crosslinking of F-actin with fascin in two different binding manners. *Cytoskeleton (Hoboken)*. 73:365-374.

Atherton, J., M. Stouffer, F. Francis, and C.A. Moores. 2018. Microtubule architecture in vitro and in cells revealed by cryo-electron tomography. *Acta Crystallogr D Struct Biol*. 74:572-584.

Baas, P.W., and M.M. Black. 1990. Individual microtubules in the axon consist of domains that differ in both composition and stability. *J Cell Biol*. 111:495-509.

Baas, P.W., and S. Lin. 2011. Hooks and comets: The story of microtubule polarity orientation in the neuron. *Dev Neurobiol*. 71:403-418.

Bakos, J., Z. Bacova, S.G. Grant, A.M. Castejon, and D. Ostatnikova. 2015. Are Molecules Involved in Neuritogenesis and Axon Guidance Related to Autism Pathogenesis? *Neuromolecular Med*. 17:297-304.

Bamburg, J.R., and D. Bray. 1987. Distribution and cellular localization of actin depolymerizing factor. *J Cell Biol*. 105:2817-2825.

Banker, G. 2018. The Development of Neuronal Polarity: A Retrospective View. *J Neurosci*. 38:1867-1873.

Bard, L., C. Boscher, M. Lambert, R.M. Mege, D. Choquet, and O. Thoumine. 2008. A molecular clutch between the actin flow and N-cadherin adhesions drives growth cone migration. *J Neurosci*. 28:5879-5890.

Bechstedt, S., K. Lu, and G.J. Brouhard. 2014. Doublecortin recognizes the longitudinal curvature of the microtubule end and lattice. *Curr Biol*. 24:2366-2375.

Bielas, S.L., F.F. Serneo, M. Chechlacz, T.J. Deerinck, G.A. Perkins, P.B. Allen, M.H. Ellisman, and J.G. Gleeson. 2007. Spinophilin facilitates dephosphorylation of doublecortin by PP1 to mediate microtubule bundling at the axonal wrist. *Cell*. 129:579-591.

Blanquie, O., and F. Bradke. 2018. Cytoskeleton dynamics in axon regeneration. *Curr Opin Neurobiol*. 51:60-69.

Bobkov, A.A., A. Muhlrad, A. Shvetsov, S. Benchaar, D. Scoville, S.C. Almo, and E. Reisler. 2004. Cofilin (ADF) affects lateral contacts in F-actin. *J Mol Biol*. 337:93-104.

Bott, C.J., L.P. McMahon, J.M. Keil, C.C. Yap, K.Y. Kwan, and B. Winckler. 2020. Nestin Selectively Facilitates the Phosphorylation of the Lissencephaly-Linked Protein Doublecortin (DCX) by cdk5/p35 to Regulate Growth Cone Morphology and Sema3a Sensitivity in Developing Neurons. *J Neurosci*. 40:3720-3740.

Bouchet-Marquis, C., B. Zuber, A.M. Glynn, M. Eltsov, M. Grabenbauer, K.N. Goldie, D. Thomas, A.S. Frangakis, J. Dubochet, and D. Chretien. 2007. Visualization of cell microtubules in their native state. *Biol Cell*. 99:45-53.

Breitsprecher, D., S.A. Koestler, I. Chizhov, M. Nemethova, J. Mueller, B.L. Goode, J.V. Small, K. Rottner, and J. Faix. 2011. Cofilin cooperates with fascin to disassemble filopodial actin filaments. *J Cell Sci*. 124:3305-3318.

Bridgman, P.C., and M.E. Dailey. 1989. The organization of myosin and actin in rapid frozen nerve growth cones. *J Cell Biol*. 108:95-109.

Brown, J.A., and P.C. Bridgman. 2009. Disruption of the cytoskeleton during Semaphorin 3A induced growth cone collapse correlates with differences in

actin organization and associated binding proteins. *Dev Neurobiol*. 69:633-646.
Brown, M.E., and P.C. Bridgman. 2003. Retrograde flow rate is increased in growth cones from myosin IIB knockout mice. *J Cell Sci*. 116:1087-1094.
Burnette, D.T., L. Ji, A.W. Schaefer, N.A. Medeiros, G. Danuser, and P. Forscher. 2008. Myosin II activity facilitates microtubule bundling in the neuronal growth cone neck. *Dev Cell*. 15:163-169.
Burnette, D.T., A.W. Schaefer, L. Ji, G. Danuser, and P. Forscher. 2007. Filopodial actin bundles are not necessary for microtubule advance into the peripheral domain of Aplysia neuronal growth cones. *Nat Cell Biol*. 9:1360-1369.
Cammarata, G.M., E.A. Bearce, and L.A. Lowery. 2016. Cytoskeletal social networking in the growth cone: How +TIPs mediate microtubule-actin cross-linking to drive axon outgrowth and guidance. *Cytoskeleton (Hoboken)*. 73:461-476.
Chakraborty, S., J. Mahamid, and W. Baumeister. 2020. Cryoelectron Tomography Reveals Nanoscale Organization of the Cytoskeleton and Its Relation to Microtubule Curvature Inside Cells. *Structure*. 28:991-1003 e1004.
Chan, C.E., and D.J. Odde. 2008. Traction dynamics of filopodia on compliant substrates. *Science*. 322:1687-1691.
Chen, M., W. Dai, S.Y. Sun, D. Jonasch, C.Y. He, M.F. Schmid, W. Chiu, and S.J. Ludtke. 2017. Convolutional neural networks for automated annotation of cellular cryo-electron tomograms. *Nat Methods*. 14:983-985.
Chretien, D., and S.D. Fuller. 2000. Microtubules switch occasionally into unfavorable configurations during elongation. *J Mol Biol*. 298:663-676.
Chretien, D., F. Metoz, F. Verde, E. Karsenti, and R.H. Wade. 1992. Lattice defects in microtubules: protofilament numbers vary within individual microtubules. *J Cell Biol*. 117:1031-1040.
Claessens, M.M., C. Semmrich, L. Ramos, and A.R. Bausch. 2008. Helical twist controls the thickness of F-actin bundles. *Proc Natl Acad Sci U S A*. 105:8819-8822.
Cohan, C.S., E.A. Welnhofer, L. Zhao, F. Matsumura, and S. Yamashiro. 2001. Role of the actin bundling protein fascin in growth cone morphogenesis: localization in filopodia and lamellipodia. *Cell Motil Cytoskeleton*. 48:109-120.
Corbo, J.C., T.A. Deuel, J.M. Long, P. LaPorte, E. Tsai, A. Wynshaw-Boris, and C.A. Walsh. 2002. Doublecortin is required in mice for lamination of the hippocampus but not the neocortex. *J Neurosci*. 22:7548-7557.
Cuveillier, C., J. Delaroche, M. Seggio, S. Gory-Faure, C. Bosc, E. Denarier, M. Bacia, G. Schoehn, H. Mohrbach, I. Kulic, A. Andrieux, I. Arnal, and C. Delphin. 2020. MAP6 is an intraluminal protein that induces neuronal microtubules to coil. *Sci Adv*. 6:eaaz4344.
Dent, E.W., S.L. Gupton, and F.B. Gertler. 2011. The growth cone cytoskeleton in axon outgrowth and guidance. *Cold Spring Harb Perspect Biol*. 3.
Deuel, T.A., J.S. Liu, J.C. Corbo, S.Y. Yoo, L.B. Rorke-Adams, and C.A. Walsh. 2006. Genetic interactions between doublecortin and doublecortin-like kinase in neuronal migration and axon outgrowth. *Neuron*. 49:41-53.
Edson, K.J., S.S. Lim, G.G. Borisy, and P.C. Letourneau. 1993. FRAP analysis of the stability of the microtubule population along the neurites of chick sensory neurons. *Cell Motil Cytoskeleton*. 25:59-72.
Edwards, R.A., and J. Bryan. 1995. Fascins, a family of actin bundling proteins. *Cell Motil Cytoskeleton*. 32:1-9.

Efimova, N., C. Yang, J.X. Chia, N. Li, C.J. Lengner, K.L. Neufeld, and T.M. Svitkina. 2020. Branched actin networks are assembled on microtubules by adenomatous polyposis coli for targeted membrane protrusion. *J Cell Biol*. 219.

Erickson, H.P. 2009. Size and shape of protein molecules at the nanometer level determined by sedimentation, gel filtration, and electron microscopy. *Biol Proced Online*. 11:32-51.

Ettinger, A., J. van Haren, S.A. Ribeiro, and T. Wittmann. 2016. Doublecortin Is Excluded from Growing Microtubule Ends and Recognizes the GDP-Microtubule Lattice. *Curr Biol*. 26:1549-1555.

Forscher, P., and S.J. Smith. 1988. Actions of cytochalasins on the organization of actin filaments and microtubules in a neuronal growth cone. *J Cell Biol*. 107:1505-1516.

Foster, H.E., C. Ventura Santos, and A.P. Carter. 2021. A cryo-ET study of microtubules in axons. *BioRxiv [Preprint]*. 2021.03.29.437471.

Francis, F., A. Koulakoff, D. Boucher, P. Chafey, B. Schaar, M.C. Vinet, G. Friocourt, N. McDonnell, O. Reiner, A. Kahn, S.K. McConnell, Y. Berwald-Netter, P. Denoulet, and J. Chelly. 1999. Doublecortin is a developmentally regulated, microtubule-associated protein expressed in migrating and differentiating neurons. *Neuron*. 23:247-256.

Friocourt, G., A. Koulakoff, P. Chafey, D. Boucher, F. Fauchereau, J. Chelly, and F. Francis. 2003. Doublecortin functions at the extremities of growing neuronal processes. *Cereb Cortex*. 13:620-626.

Fu, X., K.J. Brown, C.C. Yap, B. Winckler, J.K. Jaiswal, and J.S. Liu. 2013. Doublecortin (Dcx) family proteins regulate filamentous actin structure in developing neurons. *J Neurosci*. 33:709-721.

Galkin, V.E., A. Orlova, D.S. Kudryashov, A. Solodukhin, E. Reisler, G.F. Schroder, and E.H. Egelman. 2011. Remodeling of actin filaments by ADF/cofilin proteins. *Proc Natl Acad Sci U S A*. 108:20568-20572.

Galkin, V.E., A. Orlova, N. Lukoyanova, W. Wriggers, and E.H. Egelman. 2001. Actin depolymerizing factor stabilizes an existing state of F-actin and can change the tilt of F-actin subunits. *J Cell Biol*. 153:75-86.

Garvalov, B.K., B. Zuber, C. Bouchet-Marquis, M. Kudryashev, M. Gruska, M. Beck, A. Leis, F. Frischknecht, F. Bradke, W. Baumeister, J. Dubochet, and M. Cyrklaff. 2006. Luminal particles within cellular microtubules. *J Cell Biol*. 174:759-765.

Geraldo, S., and P.R. Gordon-Weeks. 2009. Cytoskeletal dynamics in growth-cone steering. *J Cell Sci*. 122:3595-3604.

Geraldo, S., U.K. Khanzada, M. Parsons, J.K. Chilton, and P.R. Gordon-Weeks. 2008. Targeting of the F-actin-binding protein drebrin by the microtubule plus-tip protein EB3 is required for neuritogenesis. *Nat Cell Biol*. 10:1181-1189.

Gordon-Weeks, P.R. 1991. Evidence for microtubule capture by filopodial actin filaments in growth cones. *Neuroreport*. 2:573-576.

Grant, T., and N. Grigorieff. 2015. Measuring the optimal exposure for single particle cryo-EM using a 2.6 A reconstruction of rotavirus VP6. *Elife*. 4:e06980.

Griffin, J.M., and F. Bradke. 2020. Therapeutic repair for spinal cord injury: combinatory approaches to address a multifaceted problem. *EMBO Mol Med*. 12:e11505.

Guha, S., A. Patil, H. Muralidharan, and P.W. Baas. 2021. Mini-review: Microtubule sliding in neurons. *Neurosci Lett*. 753:135867.

Gungabissoon, R.A., and J.R. Bamburg. 2003. Regulation of growth cone actin dynamics by ADF/cofilin. *J Histochem Cytochem*. 51:411-420.
Hagen, W.J.H., W. Wan, and J.A.G. Briggs. 2017. Implementation of a cryo-electron tomography tilt-scheme optimized for high resolution subtomogram averaging. *J Struct Biol*. 197:191-198.
Haviv, L., D. Gillo, F. Backouche, and A. Bernheim-Groswasser. 2008. A cytoskeletal demolition worker: myosin II acts as an actin depolymerization agent. *J Mol Biol*. 375:325-330.
Huehn, A., W. Cao, W.A. Elam, X. Liu, E.M. De La Cruz, and C.V. Sindelar. 2018. The actin filament twist changes abruptly at boundaries between bare and cofilin-decorated segments. *J Biol Chem*. 293:5377-5383.
Huehn, A.R., J.P. Bibeau, A.C. Schramm, W. Cao, E.M. De La Cruz, and C.V. Sindelar. 2020. Structures of cofilin-induced structural changes reveal local and asymmetric perturbations of actin filaments. *Proc Natl Acad Sci U S A*. 117:1478-1484.
Ishikawa, R., K. Hayashi, T. Shirao, Y. Xue, T. Takagi, Y. Sasaki, and K. Kohama. 1994. Drebrin, a development-associated brain protein from rat embryo, causes the dissociation of tropomyosin from actin filaments. *J Biol Chem*. 269:29928-29933.
Ishikawa, R., T. Sakamoto, T. Ando, S. Higashi-Fujime, and K. Kohama. 2003. Polarized actin bundles formed by human fascin-1: their sliding and disassembly on myosin II and myosin V in vitro. *J Neurochem*. 87:676-685.
Jansen, S., A. Collins, C. Yang, G. Rebowski, T. Svitkina, and R. Dominguez. 2011. Mechanism of actin filament bundling by fascin. *J Biol Chem*. 286:30087-30096.
Jean, D.C., P.W. Baas, and M.M. Black. 2012. A novel role for doublecortin and doublecortin-like kinase in regulating growth cone microtubules. *Hum Mol Genet*. 21:5511-5527.
Kahn, O.I., and P.W. Baas. 2016. Microtubules and Growth Cones: Motors Drive the Turn. *Trends Neurosci*. 39:433-440.
Kappeler, C., M. Dhenain, F. Phan Dinh Tuy, Y. Saillour, S. Marty, C. Fallet-Bianco, I. Souville, E. Souil, J.M. Pinard, G. Meyer, F. Encha-Razavi, A. Volk, C. Beldjord, J. Chelly, and F. Francis. 2007. Magnetic resonance imaging and histological studies of corpus callosal and hippocampal abnormalities linked to doublecortin deficiency. *J Comp Neurol*. 500:239-254.
Kappeler, C., Y. Saillour, J.P. Baudoin, F.P. Tuy, C. Alvarez, C. Houbron, P. Gaspar, G. Hamard, J. Chelly, C. Metin, and F. Francis. 2006. Branching and nucleokinesis defects in migrating interneurons derived from doublecortin knockout mice. *Hum Mol Genet*. 15:1387-1400.
Kim, S.W., and K.T. Kim. 2020. Expression of Genes Involved in Axon Guidance: How Much Have We Learned? *Int J Mol Sci*. 21.
Kollman, J.M., A. Merdes, L. Mourey, and D.A. Agard. 2011. Microtubule nucleation by gamma-tubulin complexes. *Nat Rev Mol Cell Biol*. 12:709-721.
Koppers, M., and G.G. Farias. 2021. Organelle distribution in neurons: Logistics behind polarized transport. *Curr Opin Cell Biol*. 71:46-54.
Kremer, J.R., D.N. Mastronarde, and J.R. McIntosh. 1996. Computer visualization of three-dimensional image data using IMOD. *J Struct Biol*. 116:71-76.
Kumari, A., S. Kesarwani, M.G. Javoor, K.R. Vinothkumar, and M. Sirajuddin. 2020. Structural insights into actin filament recognition by commonly used cellular actin markers. *EMBO J*. 39:e104006.

Kureishy, N., V. Sapountzi, S. Prag, N. Anilkumar, and J.C. Adams. 2002. Fascins, and their roles in cell structure and function. *Bioessays*. 24:350-361.
Li, P., L. Li, B. Yu, X. Wang, Q. Wang, J. Lin, Y. Zheng, J. Zhu, M. He, Z. Xia, M. Tu, J.S. Liu, Z. Lin, and X. Fu. 2021. Doublecortin facilitates the elongation of the somatic Golgi apparatus into proximal dendrites. *Mol Biol Cell*. 32:422-434.
Lord, S.J., K.B. Velle, R.D. Mullins, and L.K. Fritz-Laylin. 2020. SuperPlots: Communicating reproducibility and variability in cell biology. *J Cell Biol*. 219.
Lowery, L.A., and D. Van Vactor. 2009. The trip of the tip: understanding the growth cone machinery. *Nat Rev Mol Cell Biol*. 10:332-343.
Marsick, B.M., K.C. Flynn, M. Santiago-Medina, J.R. Bamburg, and P.C. Letourneau. 2010. Activation of ADF/cofilin mediates attractive growth cone turning toward nerve growth factor and netrin-1. *Dev Neurobiol*. 70:565-588.
McCullough, B.R., L. Blanchoin, J.L. Martiel, and E.M. De la Cruz. 2008. Cofilin increases the bending flexibility of actin filaments: implications for severing and cell mechanics. *J Mol Biol*. 381:550-558.
McGough, A., B. Pope, W. Chiu, and A. Weeds. 1997. Cofilin changes the twist of F-actin: implications for actin filament dynamics and cellular function. *J Cell Biol*. 138:771-781.
McIntosh, J.R., E. O'Toole, G. Morgan, J. Austin, E. Ulyanov, F. Ataullakhanov, and N. Gudimchuk. 2018. Microtubules grow by the addition of bent guanosine triphosphate tubulin to the tips of curved protofilaments. *J Cell Biol*. 217:2691-2708.
Medeiros, N.A., D.T. Burnette, and P. Forscher. 2006. Myosin II functions in actin-bundle turnover in neuronal growth cones. *Nat Cell Biol*. 8:215-226.
Mikati, M.A., E.E. Grintsevich, and E. Reisler. 2013. Drebrin-induced stabilization of actin filaments. *J Biol Chem*. 288:19926-19938.
Mizui, T., N. Kojima, H. Yamazaki, M. Katayama, K. Hanamura, and T. Shirao. 2009. Drebrin E is involved in the regulation of axonal growth through actin-myosin interactions. *J Neurochem*. 109:611-622.
Moores, C.A., M. Perderiset, F. Francis, J. Chelly, A. Houdusse, and R.A. Milligan. 2004. Mechanism of microtubule stabilization by doublecortin. *Mol Cell*. 14:833-839.
Mosialos, G., S. Yamashiro, R.W. Baughman, P. Matsudaira, L. Vara, F. Matsumura, E. Kieff, and M. Birkenbach. 1994. Epstein-Barr virus infection induces expression in B lymphocytes of a novel gene encoding an evolutionarily conserved 55-kilodalton actin-bundling protein. *J Virol*. 68:7320-7328.
Nicastro, D., C. Schwartz, J. Pierson, R. Gaudette, M.E. Porter, and J.R. McIntosh. 2006. The molecular architecture of axonemes revealed by cryoelectron tomography. *Science*. 313:944-948.
Paul, D.M., J. Mantell, U. Borucu, J. Coombs, K.J. Surridge, J.M. Squire, P. Verkade, and M.P. Dodding. 2020. In situ cryo-electron tomography reveals filamentous actin within the microtubule lumen. *J Cell Biol*. 219.
Pettersen, E.F., T.D. Goddard, C.C. Huang, G.S. Couch, D.M. Greenblatt, E.C. Meng, and T.E. Ferrin. 2004. UCSF Chimera--a visualization system for exploratory research and analysis. *J Comput Chem*. 25:1605-1612.
Ray, S., E. Meyhofer, R.A. Milligan, and J. Howard. 1993. Kinesin follows the microtubule's protofilament axis. *J Cell Biol*. 121:1083-1093.
Rohou, A., and N. Grigorieff. 2015. CTFFIND4: Fast and accurate defocus estimation from electron micrographs. *J Struct Biol*. 192:216-221.

Roig-Puiggros, S., R.J. Vigouroux, D. Beckman, N.I. Bocai, B. Chiou, J. Davimes, G. Gomez, S. Grassi, A. Hoque, T.K. Karikari, F. Kiffer, M. Lopez, G. Lunghi, P. Mazengenya, S. Meier, M. Olguin-Albuerne, M.M. Oliveira, J. Paraiso-Luna, J. Pradhan, A. Radiske, A.B. Ramos-Hryb, M.C. Ribeiro, R. Schellino, M.C. Selles, S. Singh, P. Theotokis, and A. Chedotal. 2020. Construction and reconstruction of brain circuits: normal and pathological axon guidance. *J Neurochem*. 153:10-32.

Roll-Mecak, A. 2020. The Tubulin Code in Microtubule Dynamics and Information Encoding. *Dev Cell*. 54:7-20.

Sabry, J.H., T.P. O'Connor, L. Evans, A. Toroian-Raymond, M. Kirschner, and D. Bentley. 1991. Microtubule behavior during guidance of pioneer neuron growth cones in situ. *J Cell Biol*. 115:381-395.

Sasaki, Y., K. Hayashi, T. Shirao, R. Ishikawa, and K. Kohama. 1996. Inhibition by drebrin of the actin-bundling activity of brain fascin, a protein localized in filopodia of growth cones. *J Neurochem*. 66:980-988.

Schaedel, L., S. Triclin, D. Chretien, A. Abrieu, C. Aumeier, J. Gaillard, L. Blanchoin, M. Thery, and K. John. 2019. Lattice defects induce microtubule self-renewal. *Nat Phys*. 15:830-838.

Schaefer, A.W., N. Kabir, and P. Forscher. 2002. Filopodia and actin arcs guide the assembly and transport of two populations of microtubules with unique dynamic parameters in neuronal growth cones. *J Cell Biol*. 158:139-152.

Schaefer, A.W., V.T. Schoonderwoert, L. Ji, N. Mederios, G. Danuser, and P. Forscher. 2008. Coordination of actin filament and microtubule dynamics during neurite outgrowth. *Dev Cell*. 15:146-162.

Sharma, S., E.E. Grintsevich, M.L. Phillips, E. Reisler, and J.K. Gimzewski. 2011. Atomic force microscopy reveals drebrin induced remodeling of f-actin with subnanometer resolution. *Nano Lett*. 11:825-827.

Sosa, H., and D. Chretien. 1998. Relationship between moire patterns, tubulin shape, and microtubule polarity. *Cell Motil Cytoskeleton*. 40:38-43.

Stiess, M., N. Maghelli, L.C. Kapitein, S. Gomis-Ruth, M. Wilsch-Brauninger, C.C. Hoogenraad, I.M. Tolic-Norrelykke, and F. Bradke. 2010. Axon extension occurs independently of centrosomal microtubule nucleation. *Science*. 327:704-707.

Stoeckli, E.T. 2018. Understanding axon guidance: are we nearly there yet? *Development*. 145.

Sun, T., and R.F. Hevner. 2014. Growth and folding of the mammalian cerebral cortex: from molecules to malformations. *Nat Rev Neurosci*. 15:217-232.

Suter, D.M., and P. Forscher. 1998. An emerging link between cytoskeletal dynamics and cell adhesion molecules in growth cone guidance. *Curr Opin Neurobiol*. 8:106-116.

Tanaka, E., T. Ho, and M.W. Kirschner. 1995. The role of microtubule dynamics in growth cone motility and axonal growth. *J Cell Biol*. 128:139-155.

Tanaka, K., S. Takeda, K. Mitsuoka, T. Oda, C. Kimura-Sakiyama, Y. Maeda, and A. Narita. 2018. Structural basis for cofilin binding and actin filament disassembly. *Nat Commun*. 9:1860.

Thery, M., and L. Blanchoin. 2021. Microtubule self-repair. *Curr Opin Cell Biol*. 68:144-154.

Tilney, L.G., J. Bryan, D.J. Bush, K. Fujiwara, M.S. Mooseker, D.B. Murphy, and D.H. Snyder. 1973. Microtubules: evidence for 13 protofilaments. *J Cell Biol*. 59:267-275.

Tint, I., D. Jean, P.W. Baas, and M.M. Black. 2009. Doublecortin associates with microtubules preferentially in regions of the axon displaying actin-rich protrusive structures. *J Neurosci*. 29:10995-11010.

Turk, M., and W. Baumeister. 2020. The promise and the challenges of cryo-electron tomography. *FEBS Lett*. 594:3243-3261.

Turonova, B., F.K.M. Schur, W. Wan, and J.A.G. Briggs. 2017. Efficient 3D-CTF correction for cryo-electron tomography using NovaCTF improves subtomogram averaging resolution to 3.4A. *J Struct Biol*. 199:187-195.

Tyler, W.J. 2012. The mechanobiology of brain function. *Nat Rev Neurosci*. 13:867-878.

Vemu, A., J. Atherton, J.O. Spector, C.A. Moores, and A. Roll-Mecak. 2017. Tubulin isoform composition tunes microtubule dynamics. *Mol Biol Cell*. 28:3564-3572.

Vitriol, E.A., A.L. Wise, M.E. Berginski, J.R. Bamburg, and J.Q. Zheng. 2013. Instantaneous inactivation of cofilin reveals its function of F-actin disassembly in lamellipodia. *Mol Biol Cell*. 24:2238-2247.

Waterman-Storer, C.M., and E.D. Salmon. 1997. Actomyosin-based retrograde flow of microtubules in the lamella of migrating epithelial cells influences microtubule dynamic instability and turnover and is associated with microtubule breakage and treadmilling. *J Cell Biol*. 139:417-434.

Williamson, T., P.R. Gordon-Weeks, M. Schachner, and J. Taylor. 1996. Microtubule reorganization is obligatory for growth cone turning. *Proc Natl Acad Sci U S A*. 93:15221-15226.

Winkelman, J.D., C. Suarez, G.M. Hocky, A.J. Harker, A.N. Morganthaler, J.R. Christensen, G.A. Voth, J.R. Bartles, and D.R. Kovar. 2016. Fascin- and alpha-Actinin-Bundled Networks Contain Intrinsic Structural Features that Drive Protein Sorting. *Curr Biol*. 26:2697-2706.

Wynshaw-Boris, A., T. Pramparo, Y.H. Youn, and S. Hirotsune. 2010. Lissencephaly: mechanistic insights from animal models and potential therapeutic strategies. *Semin Cell Dev Biol*. 21:823-830.

Yamada, H., T. Abe, A. Satoh, N. Okazaki, S. Tago, K. Kobayashi, Y. Yoshida, Y. Oda, M. Watanabe, K. Tomizawa, H. Matsui, and K. Takei. 2013. Stabilization of actin bundles by a dynamin 1/cortactin ring complex is necessary for growth cone filopodia. *J Neurosci*. 33:4514-4526.

Yang, S., F.K. Huang, J. Huang, S. Chen, J. Jakoncic, A. Leo-Macias, R. Diaz-Avalos, L. Chen, J.J. Zhang, and X.Y. Huang. 2013. Molecular mechanism of fascin function in filopodial formation. *J Biol Chem*. 288:274-284.

Zhang, X.F., A.W. Schaefer, D.T. Burnette, V.T. Schoonderwoert, and P. Forscher. 2003. Rho-dependent contractile responses in the neuronal growth cone are independent of classical peripheral retrograde actin flow. *Neuron*. 40:931-944.

Zheng, S.Q., E. Palovcak, J.P. Armache, K.A. Verba, Y. Cheng, and D.A. Agard. 2017. MotionCor2: anisotropic correction of beam-induced motion for improved cryo-electron microscopy. *Nat Methods*. 14:331-332.

Zhou, F.Q., C.M. Waterman-Storer, and C.S. Cohan. 2002. Focal loss of actin bundles causes microtubule redistribution and growth cone turning. *J Cell Biol*. 157:839-849.

Figure 1

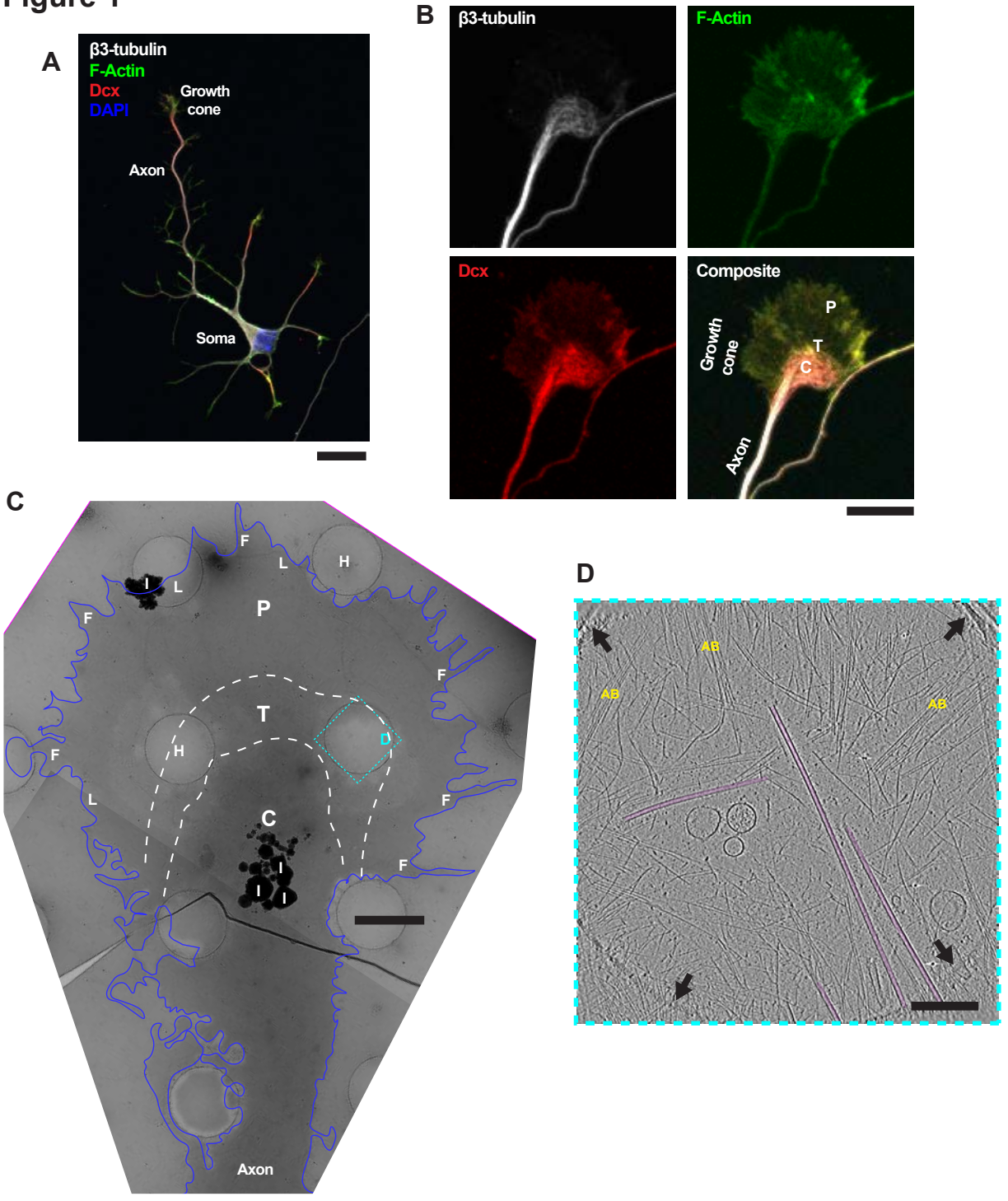
A
β3-tubulin
F-Actin
Dcx
DAPI
Growth cone
Axon
Soma
B
β3-tubulin
F-Actin
Dcx
Composite
P
T
C
Growth cone
Axon
C
F
L
H
I
P
T
D
C
Axon
D
AB

Figure 2

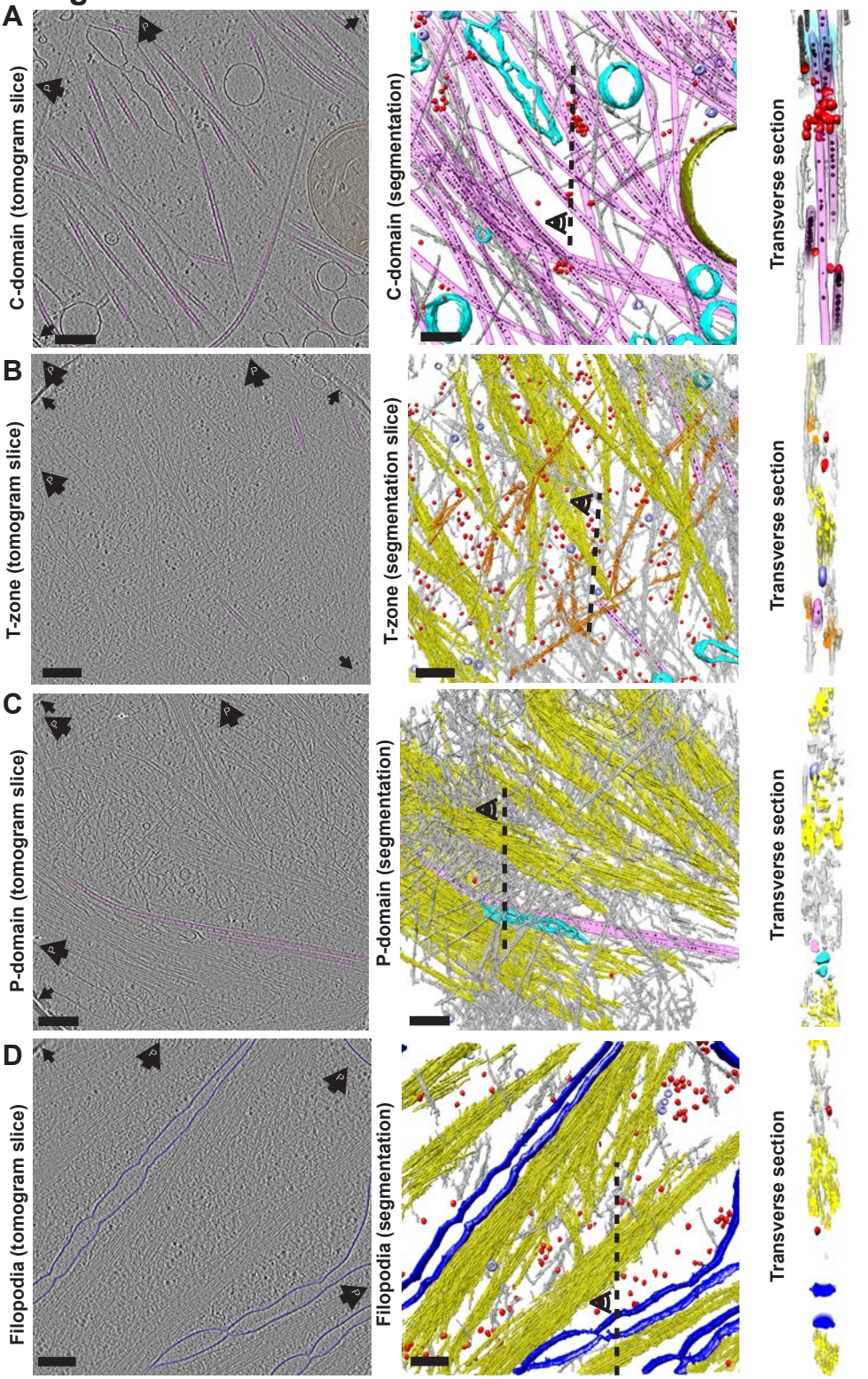
A
C-domain (tomogram slice)
C-domain (segmentation)
Transverse section
B
T-zone (tomogram slice)
T-zone (segmentation slice)
Transverse section
C
P-domain (tomogram slice)
P-domain (segmentation)
Transverse section
D
Filopodia (tomogram slice)
Filopodia (segmentation)
Transverse section

Figure 3

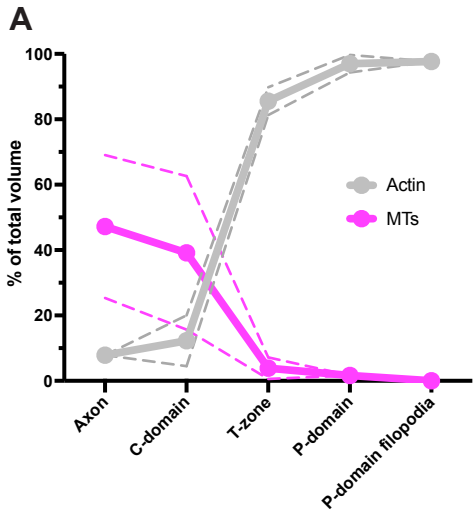
A
% of total volume
100
80
60
40
20
0
Actin
MTs
Axon
C-domain
T-zone
P-domain
P-domain filopodia

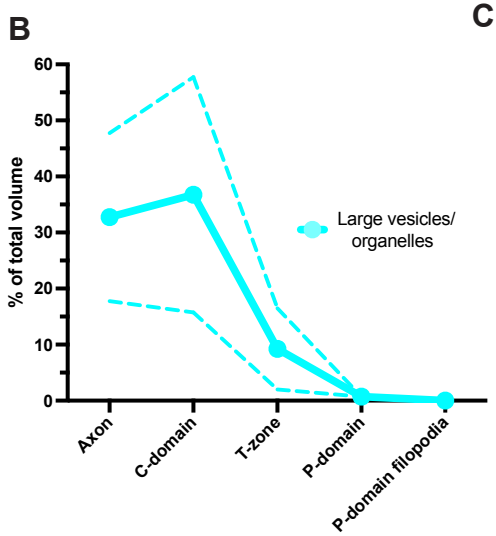
B
% of total volume
60
50
40
30
20
10
0
Large vesicles/
organelles
Axon
C-domain
T-zone
P-domain
P-domain filopodia

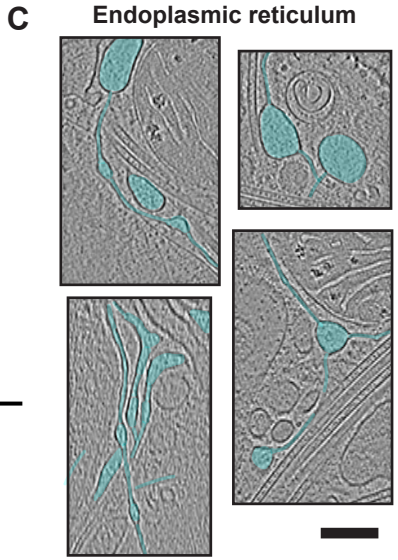
C
Endoplasmic reticulum

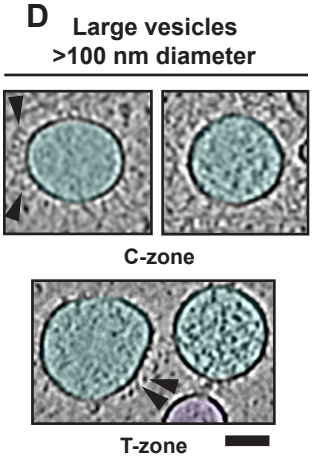
D
Large vesicles
>100 nm diameter
C-zone
T-zone

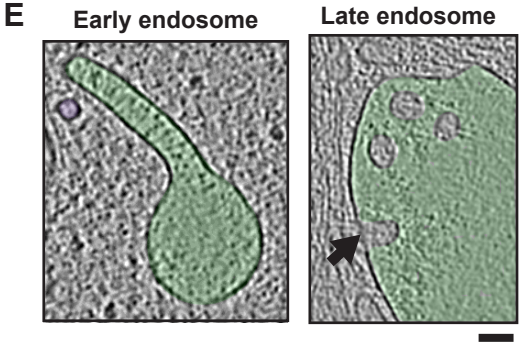
E
Early endosome
Late endosome

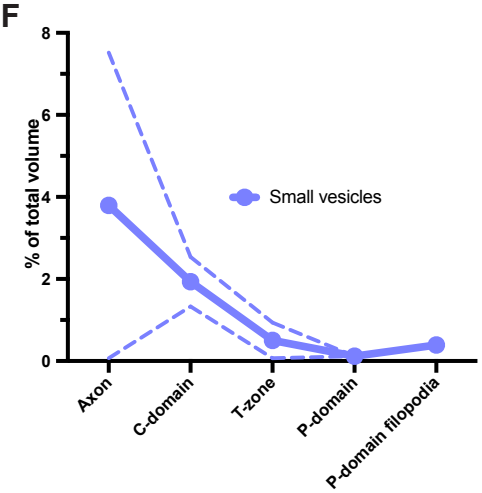
F
% of total volume
8
6
4
2
0
Small vesicles
Axon
C-domain
T-zone
P-domain
P-domain filopodia

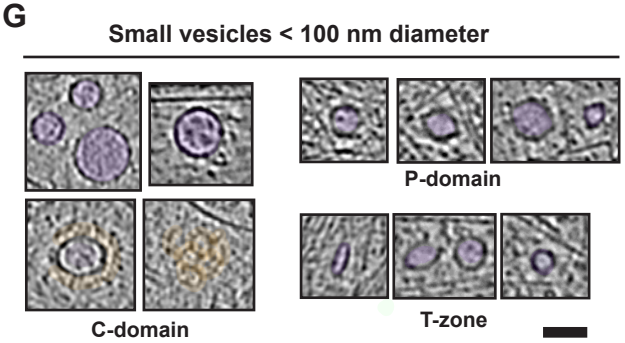
G
Small vesicles < 100 nm diameter
P-domain
C-domain
T-zone

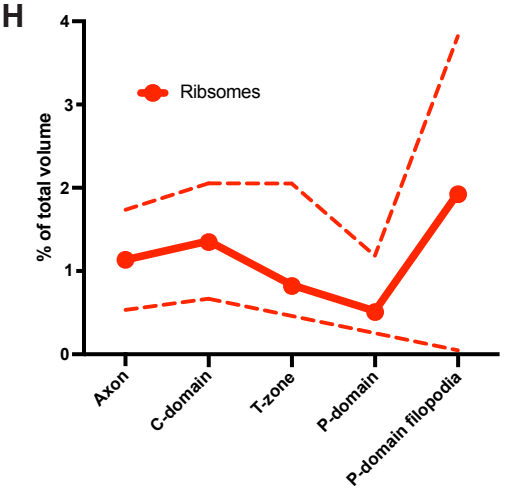
H
% of total volume
4
3
2
1
0
Ribsomes
Axon
C-domain
T-zone
P-domain
P-domain filopodia

Figure 4

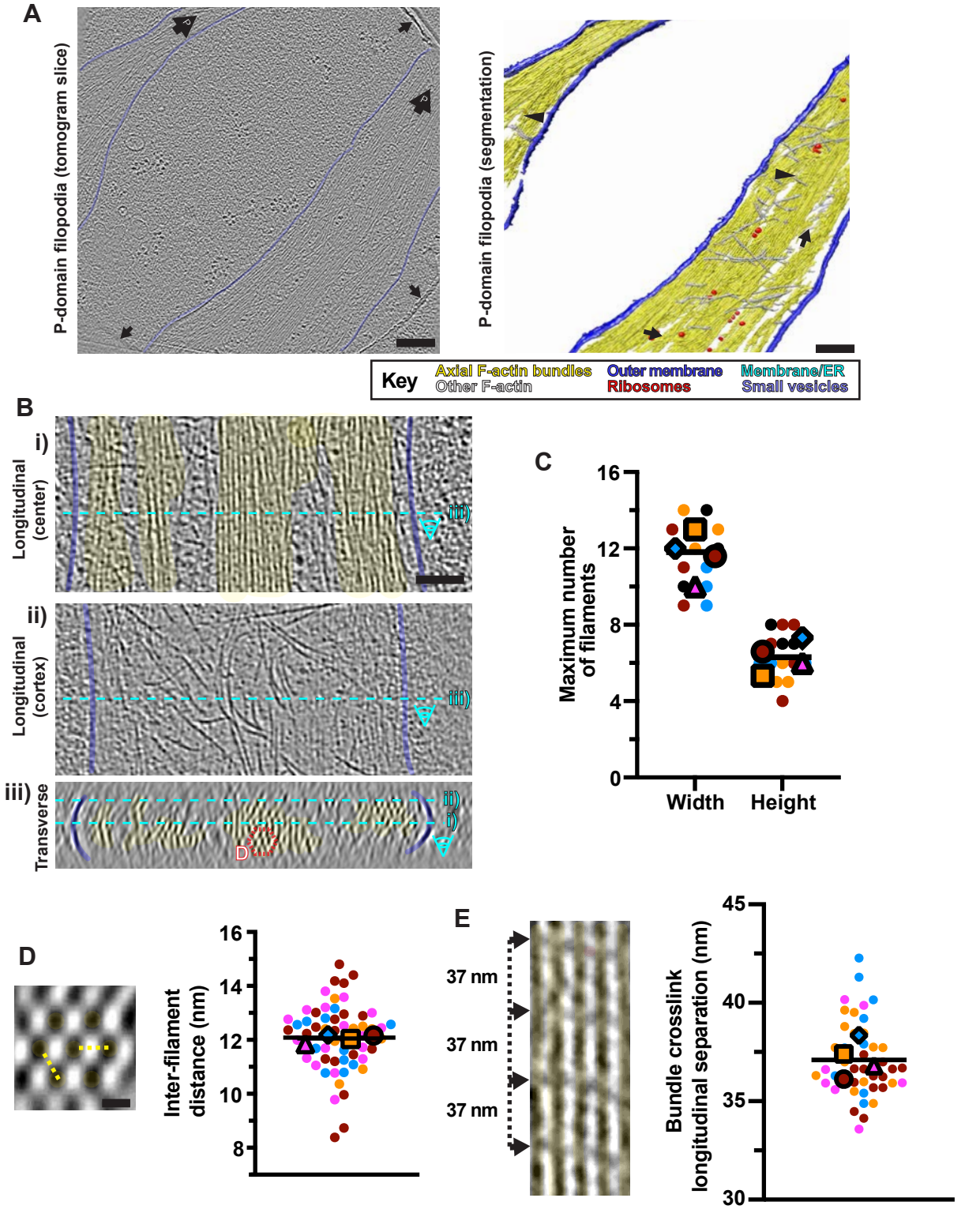
A
P-domain filopodia (tomogram slice)
P-domain filopodia (segmentation)
Key
Axial F-actin bundles
Other F-actin
Outer membrane
Ribosomes
Membrane/ER
Small vesicles
B
i)
Longitudinal (center)
ii)
Longitudinal (cortex)
iii)
Transverse
C
Maximum number of filaments
16
12
8
4
0
Width
Height
D
Inter-filament distance (nm)
16
14
12
10
8
E
37 nm
37 nm
37 nm
Bundle crosslink longitudinal separation (nm)
45
40
35
30

Figure 5

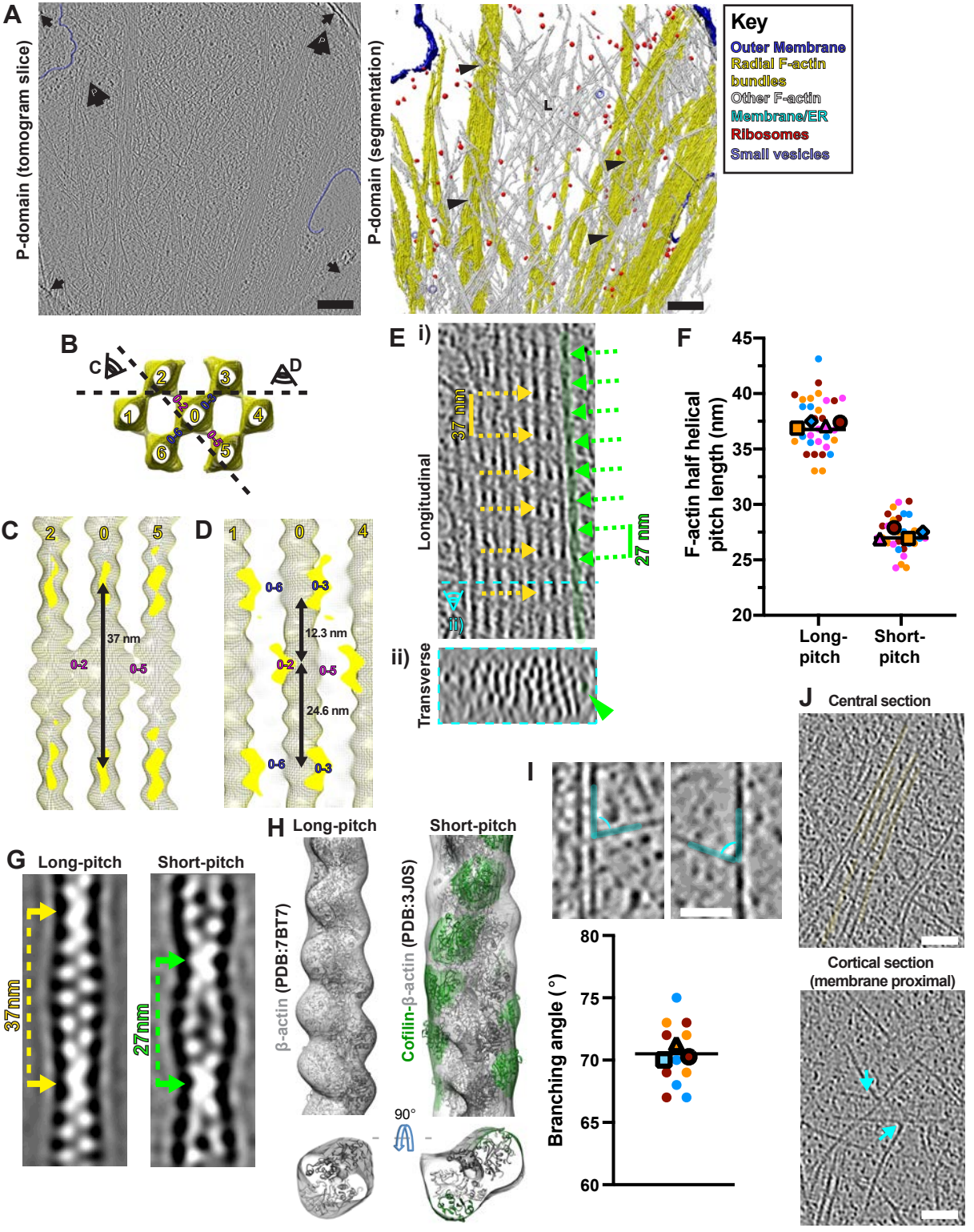
A
P-domain (tomogram slice)
P-domain (segmentation)
Key
Outer Membrane
Radial F-actin bundles
Other F-actin
Membrane/ER
Ribosomes
Small vesicles
B
C
D
E
i)
ii)
Longitudinal
Transverse
37 nm
27 nm
F
F-actin half helical pitch length (nm)
Long-pitch
Short-pitch
G
Long-pitch
Short-pitch
37nm
27nm
H
Long-pitch
Short-pitch
β-actin (PDB:7BT7)
Cofilin-β-actin (PDB:3J0S)
90°
I
Branching angle (°)
J
Central section
Cortical section (membrane proximal)

Figure 6

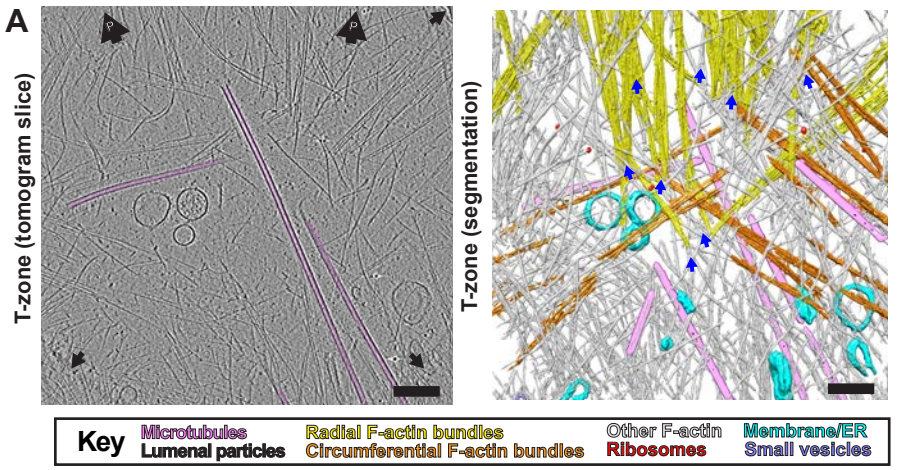
A
T-zone (tomogram slice)
T-zone (segmentation)
Key
Microtubules
Lumenal particles
Radial F-actin bundles
Circumferential F-actin bundles
Other F-actin
Ribosomes
Membrane/ER
Small vesicles

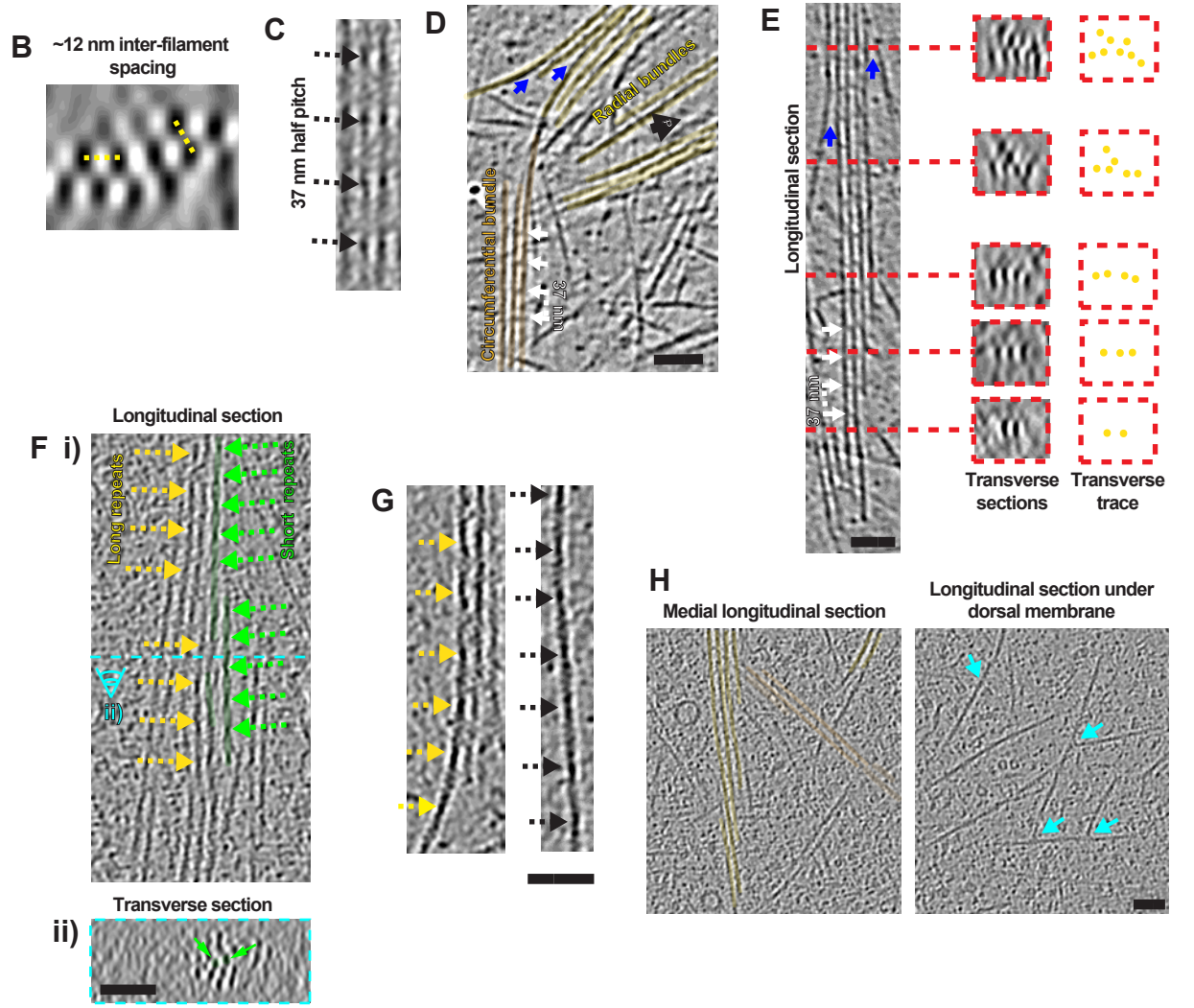
B
~12 nm inter-filament spacing
C
37 nm half pitch
D
Radial bundles
Circumferential bundle
37 nm
E
Longitudinal section
37 nm
Transverse sections
Transverse trace
F i)
Longitudinal section
Long repeats
Short repeats
ii)
Transverse section
G
H
Medial longitudinal section
Longitudinal section under dorsal membrane

Figure 7

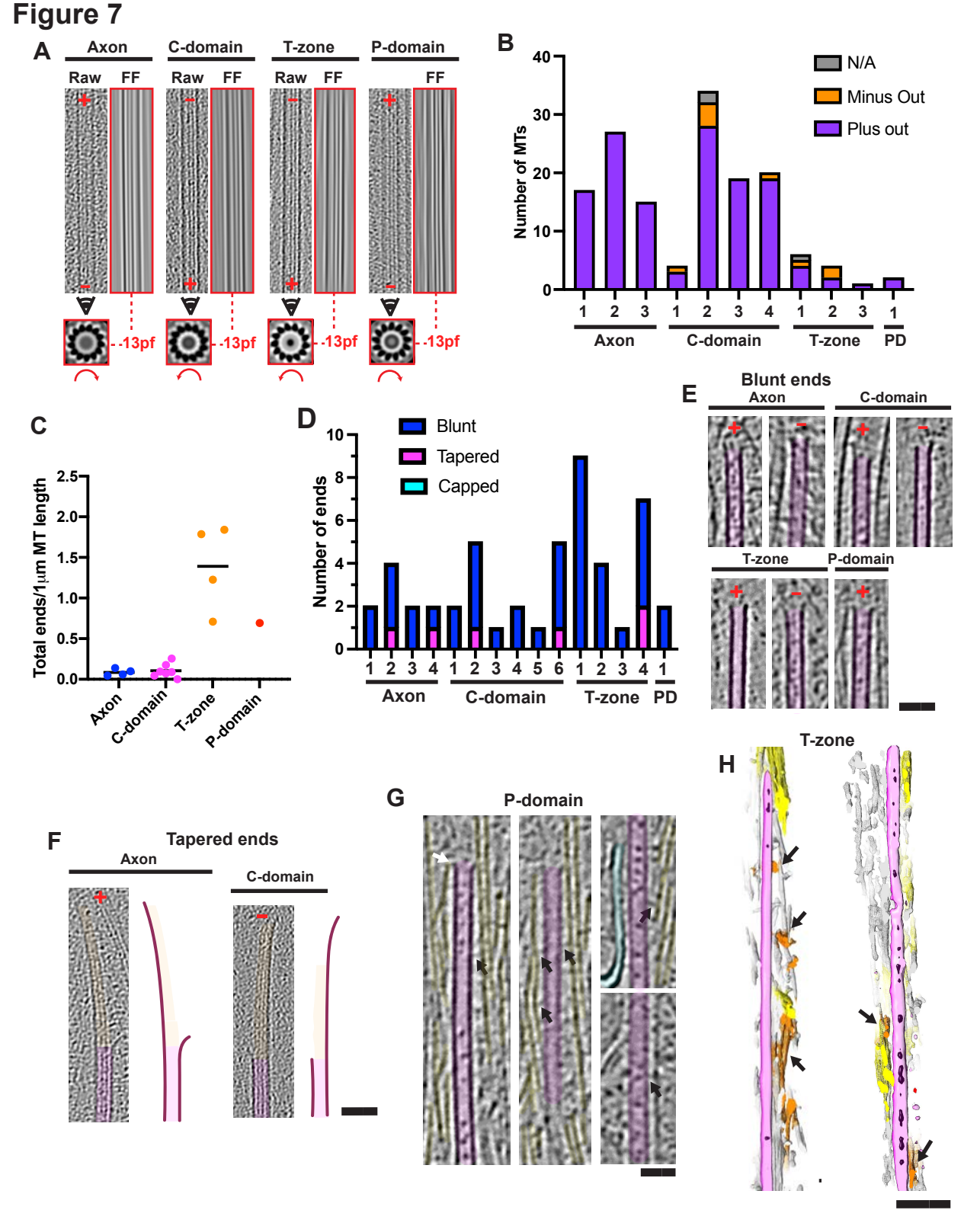
A
Axon
C-domain
T-zone
P-domain
Raw
FF
13pf
B
N/A
Minus Out
Plus out
Number of MTs
Axon
C-domain
T-zone
PD
C
Total ends/1μm MT length
Axon
C-domain
T-zone
P-domain
D
Blunt
Tapered
Capped
Number of ends
Axon
C-domain
T-zone
PD
E
Blunt ends
Axon
C-domain
T-zone
P-domain
F
Tapered ends
Axon
C-domain
G
P-domain
H
T-zone

Figure 8

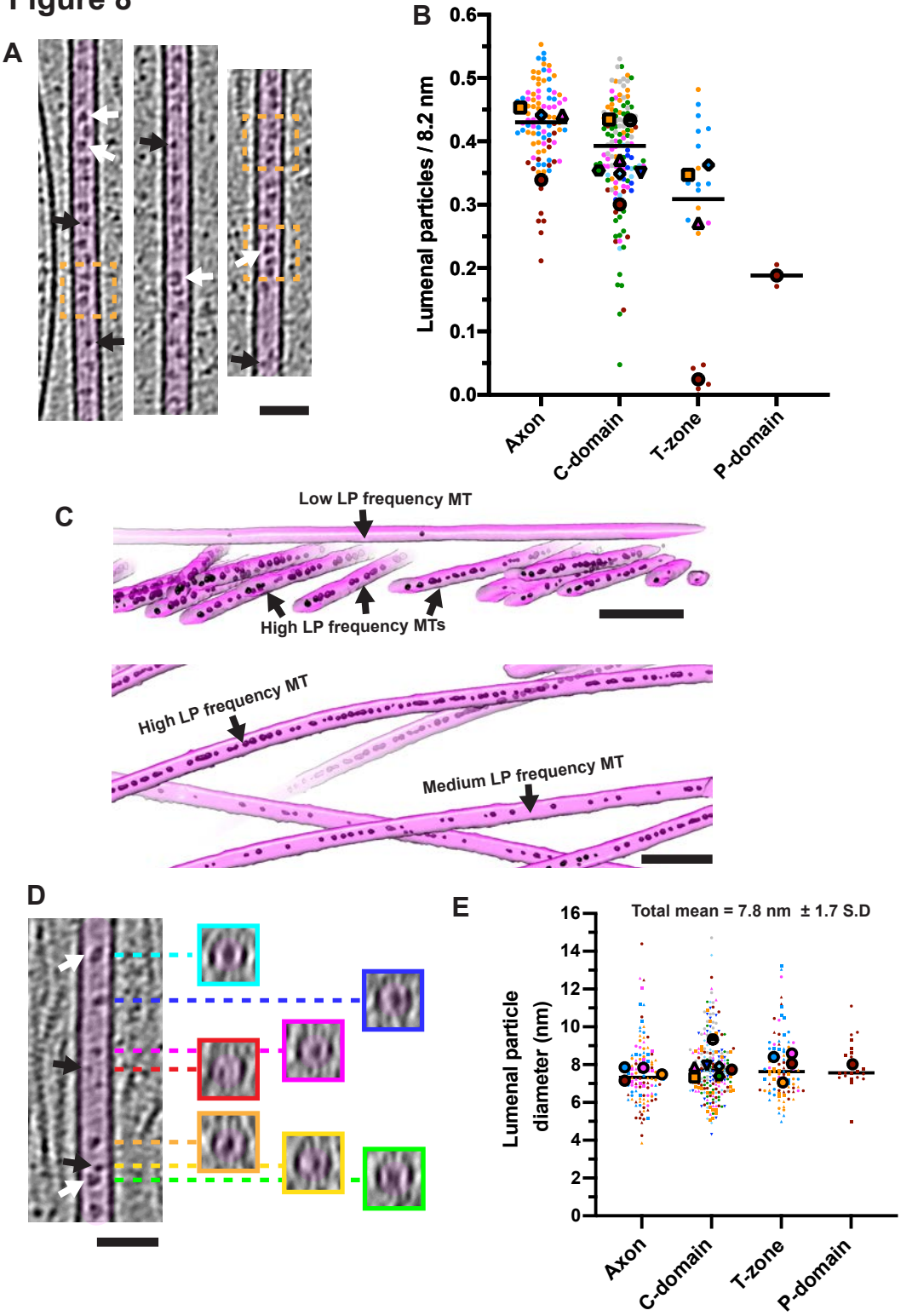
A
B
Lumenal particles / 8.2 nm
0.6
0.5
0.4
0.3
0.2
0.1
0.0
Axon
C-domain
T-zone
P-domain
C
Low LP frequency MT
High LP frequency MTs
High LP frequency MT
Medium LP frequency MT
D
E
Total mean = 7.8 nm ± 1.7 S.D
Lumenal particle diameter (nm)
16
14
12
10
8
6
4
2
0
Axon
C-domain
T-zone
P-domain

Figure 9

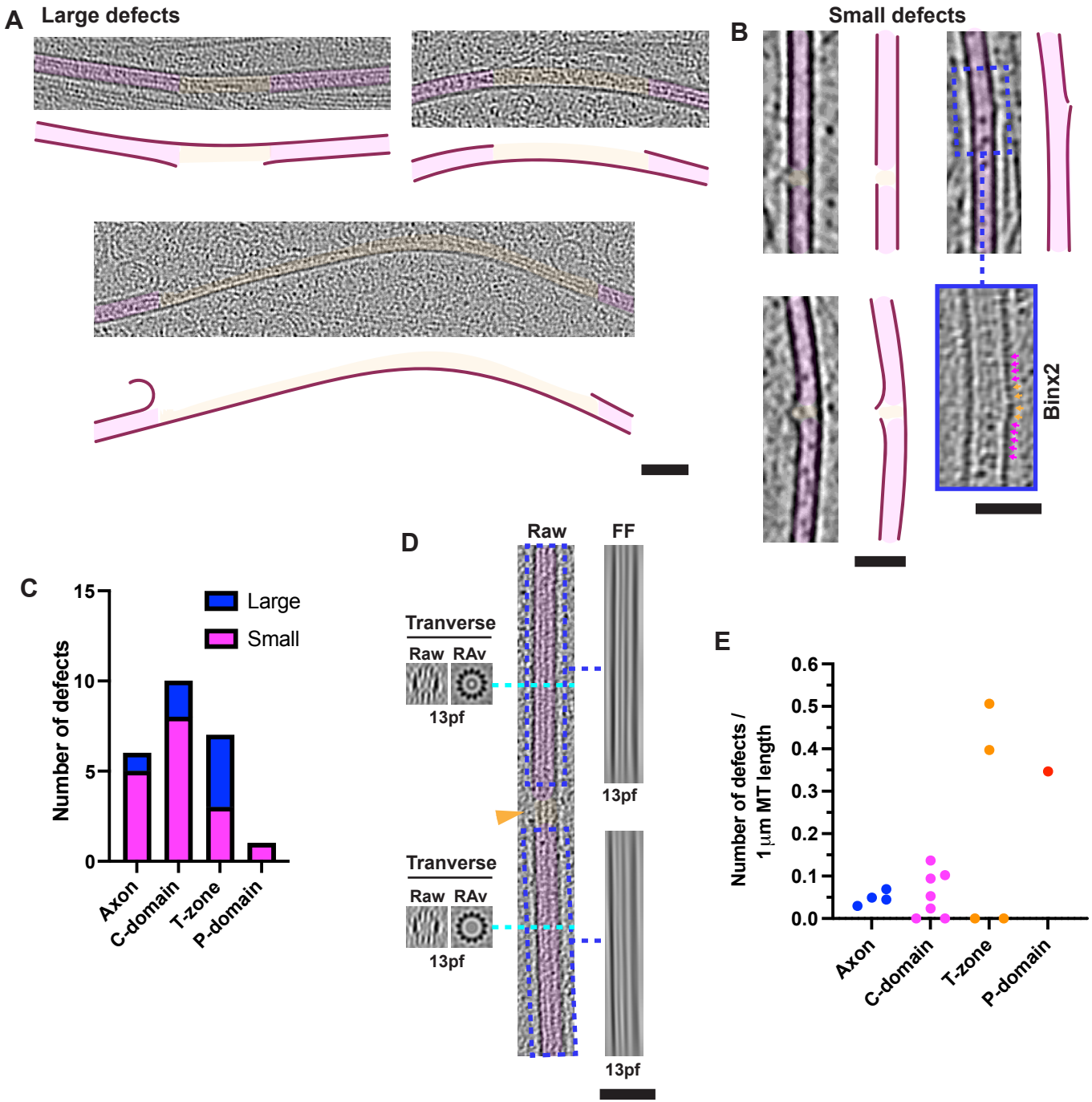
A
Large defects
B
Small defects
Binx2
C
Large
Small
Number of defects
15
10
5
0
Axon
C-domain
T-zone
P-domain
D
Raw
FF
Tranverse
Raw
RAv
13pf
13pf
Tranverse
Raw
RAv
13pf
13pf
E
Number of defects / 1 μm MT length
0.6
0.5
0.4
0.3
0.2
0.1
0.0
Axon
C-domain
T-zone
P-domain

Figure 10

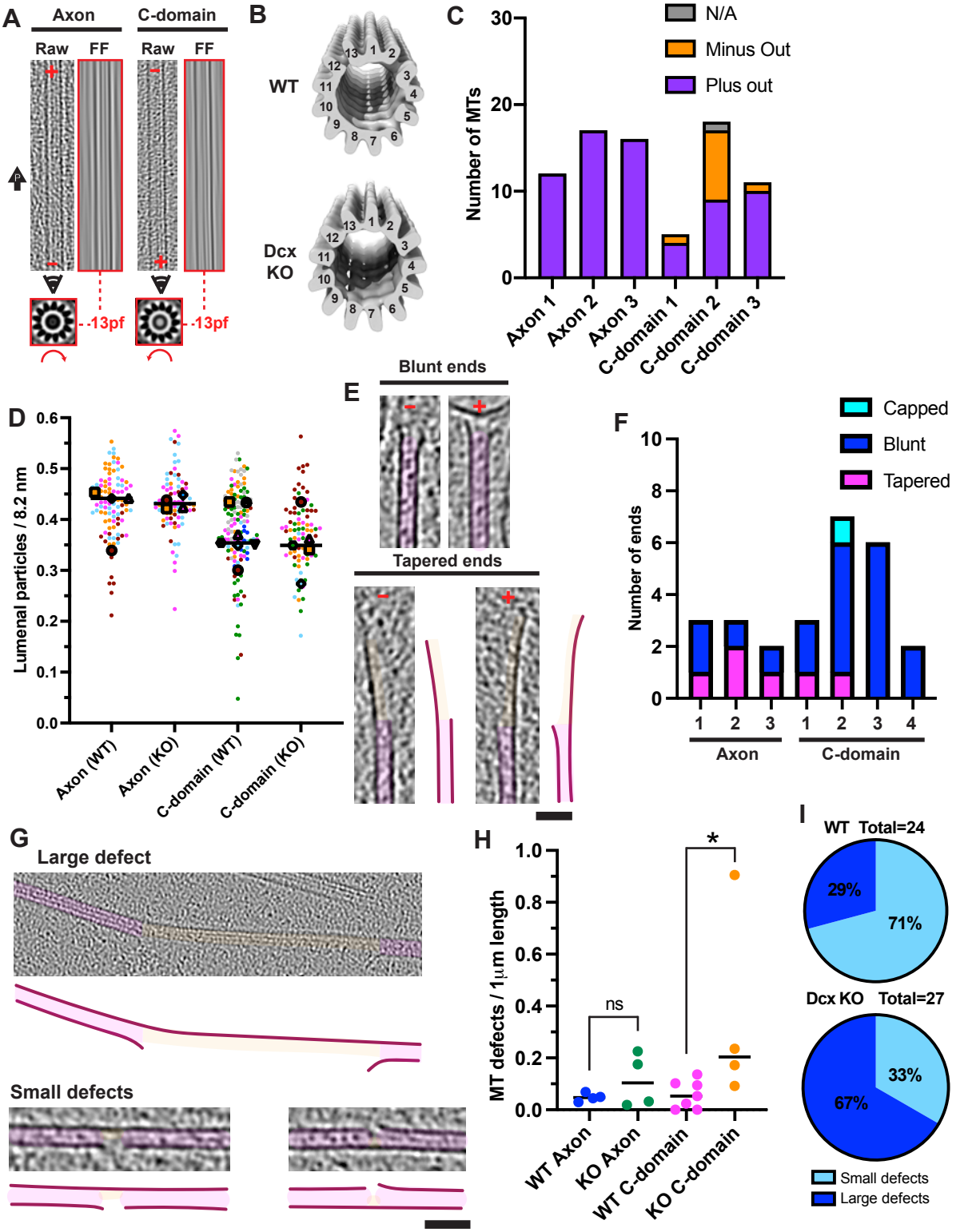
A
Axon
C-domain
Raw
FF
Raw
FF
-13pf
-13pf
B
WT
Dcx KO
C
N/A
Minus Out
Plus out
Number of MTs
Axon 1
Axon 2
Axon 3
C-domain 1
C-domain 2
C-domain 3
D
Lumenal particles / 8.2 nm
Axon (WT)
Axon (KO)
C-domain (WT)
C-domain (KO)
E
Blunt ends
Tapered ends
F
Capped
Blunt
Tapered
Number of ends
Axon
C-domain
G
Large defect
Small defects
H
MT defects / 1µm length
ns
*
WT Axon
KO Axon
WT C-domain
KO C-domain
I
WT Total=24
29%
71%
Dcx KO Total=27
33%
67%
Small defects
Large defects